Scholl, D., Wang, Y., Sheppard, D. N., Govaerts, C., & al., E. (2021). A Topological Switch in CFTR Modulates Channel Activity and Sensitivity to Unfolding. *Nature Chemical Biology*, *17*(9), 989-997. https://doi.org/10.1038/s41589-021-00844-0

A Topological Switch in CFTR Modulates Channel Activity and Sensitivity to Unfolding

Daniel Scholl[1], Maud Sigoillot[1], Marie Overtus[1], Rafael Colomer Martinez[1], Chloé Martens[1], Yiting Wang[2], Els Pardon[3,4], Toon Laeremans[3,4], Abel Garcia-Pino[5], Jan Steyaert[3,4], David N. Sheppard[2], Jelle Hendrix[6,7], Cédric Govaerts[1]*

[1]: SFMB, Université Libre de Bruxelles (ULB) CP206/02, Boulevard du Triomphe, Building BC, B-1050 Brussels, Belgium

[2]: School of Physiology, Pharmacology and Neuroscience, University of Bristol, Bristol BS8 1TD, UK

[3]: VIB-VUB center for Structural Biology, VIB, Pleinlaan 2, B-1050 Brussels, Belgium

[4]: Structural Biology Brussels, Vrije Universiteit Brussel (VUB), Pleinlaan 2, B-1050 Brussels, Belgium

[5]: Cellular and Molecular Microbiology, Université Libre de Bruxelles (ULB), B-6041, Gosselies, Belgium

[6]: Dynamic Bioimaging Lab, Advanced Optical Microscopy Centre and Biomedical Research Institute, Hasselt University, Agoralaan C (BIOMED), B-3590 Diepenbeek, Belgium

[7]: Molecular Imaging and Photonics, Chemistry Department, KU Leuven, Celestijnenlaan 200F (Chem&Tech), B-3001 Leuven, Belgium

*To whom correspondence should be addressed. E-mail: Cedric.Govaerts@ulb.ac.be.

Abstract

The cystic fibrosis transmembrane conductance regulator (CFTR) anion channel is essential to maintain fluid homeostasis in key organs. Functional impairment of CFTR due to mutations in the cftr gene leads to Cystic Fibrosis (CF). Here we show that the first nucleotide-binding domain (NBD1) of CFTR can spontaneously adopt an alternative conformation that departs from the canonical NBD fold previously observed for CFTR and related transporters. Crystallography studies reveal that this conformation involves a topological reorganization of NBD1. Single-molecule fluorescence resonance energy transfer microscopy shows that the equilibrium between the conformations is regulated by ATP binding. However, under destabilizing conditions, such as the prominent disease-causing mutation F508el, this conformational flexibility enables unfolding of the β-subdomain. Our data indicate that in wild-type CFTR this conformational transition of NBD1 regulates channel function, but, in the presence of the F508del mutation, it allows domain misfolding and subsequent protein degradation. Our work provides a framework to design conformation-specific therapeutics to prevent noxious transitions.

Introduction

Cystic fibrosis (CF) is caused by mutations in the cystic fibrosis transmembrane conductance regulator (CFTR) anion channel that lead to impaired epithelial ion transport with dramatic consequences in multiple organs, particularly the lungs[1,2]. CFTR belongs to the family of ATP-binding cassette (ABC) transporters, with a pseudo-dimeric architecture comprising 12 transmembrane helices connected to two nucleotide-binding domains (NBDs)[3], as illustrated in Fig. 1A. In most CF patients, the disease is caused by deletion of the phenylalanine residue at position 508 (F508del) in NBD1, which leads to absence of the channel from the plasma membrane[4]. On the one hand, the mutation is known to perturb assembly of this multidomain protein[5–8]. On the other hand, studies have shown that F508del compromises CFTR by decreasing the thermal stability of NBD1 and subsequently of the entire protein[6,9]. At physiological temperatures, the mutant channel is rapidly recognized as misfolded and is degraded by the cellular quality control system[10,11] abolishing maturation and cell-surface expression. *In vitro* studies demonstrate that F508del has little effect on the NBD1 structure per se, but rather alters stability and dynamics of the domain[6,12,13]. Yet, the molecular events that lead to NBD1 misfolding remain poorly understood. We can gain molecular insight from stabilizing mutations that compensate for the effects of F508del and lead to recovery of membrane expression and channel function[14–16]. For example, by studying CFTR from different species, it has been shown that replacing residues S492, A534 and I539 in the human channel by their avian counterparts largely suppresses the deleterious effects of F508del[15]. Another striking example where a sequence change rescues the mutant protein involves the regulatory insertion (RI), a 32-residue long segment found in NBD1 of all CFTR orthologs yet absent in related ABC transporters. The role of the RI has remained obscure. It is not resolved in crystal structures of NBD1[12,17,18] nor cryo-EM structures[3,19,20] of full-length CFTR and has been described as intrinsically disordered[13]. Remarkably, removal of the RI increases the stability of isolated NBD1 and, in the context of F508del-CFTR, largely recovers maturation, cell surface expression, activity and interdomain assembly of the mutant channel[21]. Another key factor is binding of ATP to NBD1, which is required for correct conformational maturation of CFTR[22] and counterbalances destabilization by F508del to some degree[7,23]. While the Walker B motif in NBD1 lacks a catalytic base[17], making this ATP-binding site non-hydrolytic[24], ATP binding is proposed to drive opening of phosphorylated CFTR channels by promoting the formation of a NBD1:NBD2 dimer[25]. We set out to examine how factors such as ATP, stabilizing mutations or removal of the RI impact the conformational landscape of NBD1 to understand the molecular origins of CF and inform therapeutic development.

Using single molecule Förster resonance energy transfer (smFRET) and nanobody-enabled structural studies, we captured and characterized a previously unknown conformation that exhibits significant structural rearrangements compared to the 'canonical' state of NBD1 originally described. We show that this non-canonical conformation confers enhanced channel activity on wild-type CFTR. Using smFRET and hydrogen deuterium exchange coupled to mass spectrometry, we characterized the conformational equilibrium between the two states of NBD1. We identify the molecular determinants of the equilibrium and show that the conformational transitions also favour local unfolding of NBD1 in the presence of the F508del mutation, elucidating the conformational pathway involved in the pathogenesis of CF.

Results

The Regulatory Insertion Adopts Distinct Conformations

We characterized the conformational landscape of the RI using smFRET which monitors the distance between individual donor and acceptor dyes covalently attached to engineered cysteines in purified NBD1 (Extended Data Figure 1).

To overcome the poor expression and stability of NBD1 from wild-type human CFTR, we used the 2PT-NBD1 variant containing three stabilizing mutations found in avian CFTR (S492P, A534P and I539T)[15]. Guided by previous studies of a functional full-length cysteine-less CFTR variant[26,27], we replaced endogenous cysteines in 2PT-NBD1. Subsequently, for each FRET reporter, we introduced a pair of cysteines at desired locations and labelled the purified variants with ATTO488 and Alexa647 as donor and acceptor fluorophores, respectively.

To monitor movements of the RI, we labelled position 426 within the RI (residues 405-436, red dashed line in Fig. 1B) and residue 519 within a structured α-helix. The FRET efficiency between this 426-519 pair showed a broad distribution of FRET states with a major population centred around E_{FRET} = 0.4 and two minor populations at E_{FRET} = 0.7 and E_{FRET} = 0.9 when measured at room temperature (22 °C) in a buffer containing 2 mM ATP (Fig. 1C). In the absence of ATP, we observed a dramatic change in the conformational profile as the entire population was shifted to E_{FRET} values centred around 0.7 and 0.9 (Fig. 1D). To assess whether conformational transitions occur on the submillisecond timescale, we generated two-dimensional (2D) plots of donor lifetime versus FRET efficiency. The relationship between donor lifetime and FRET efficiency depends on the kinetics of the conformational changes relative to the observation time[28]. Specifically, if the signals fall on the *static FRET line* (red line in Fig. 1E), there is no conformational exchange during the passage of the protein through the confocal volume of the smFRET microscope (~1–5 ms), indicating that the protein exists in one conformation at a time. By contrast, if the signals fall above the static FRET line structural changes occur, indicating dynamics on the submillisecond timescale. For the 426-519 reporter pair, we observed that the population at E_{FRET} = 0.4 falls on the static FRET line and thus is long-lived while the populations at 0.7 and 0.9 fall off the static FRET line and appear to be dynamic (Fig. 1E-F). These two states can be better separated using 2D histograms of FRET efficiency versus acceptor lifetime (Extended Data Figure 2).

To characterize the structural changes between the low and high FRET states, we screened a library of nanobodies directed against 2PT-NBD1[29] to identify RI-conformation specific binders. We identified a nanobody termed G11a which, upon binding to 2PT-NBD1, restricted the conformation of the RI to the high FRET state at E_{FRET} = 0.9 (Fig. 1G). We observed similar high FRET (Figs. 1E-F) and acceptor lifetime (Extended Data Figure 2D) values in the absence of the nanobody. This suggests that the nanobody does not induce new conformations of 2PT-NBD1, but rather stabilizes a protein state which is naturally present in the conformational ensemble.

To summarize, smFRET measurements demonstrated that the conformational space of the RI encompasses several preferred states whose relative populations are regulated by ATP binding.

Nanobody G11a Stabilizes an Alternative Conformation of NBD1

We characterized the biophysical and biochemical properties of nanobody G11a and observed that it stabilizes 2PT-NBD1 upon binding, increasing its melting temperature by 10 °C in differential scanning fluorescence (DSF) experiments (Extended Data Figure 3 and Supplementary Table 1). By contrast, G11a binding was lost with the ΔRI-NBD1 variant where residues 405–436 have been removed, suggesting that G11a interacts directly with part of the RI or binds a conformation adopted only in presence of the RI (Extended Data Figure 3B). We determined the high-resolution crystal structure of the 2PT-NBD1:G11a complex (Fig. 2A) at 2.7 Å (Supplementary Table 2) and found that the binding epitope includes several residues of the RI (residues 423–436, red), as well as part of strand S4 (residues 476–487, blue). The conformation of NBD1 captured by G11a is characterized by extensive structural changes in the β-subdomain resulting in an alternative topology compared to the previously published crystal structures of NBD1 of CFTR[12,17] and other ABC proteins (Fig. 2B-C).

All structures of human NBD1 published so far display a similar fold[12,17,18]. In this canonical conformation (Fig. 2C), the β-subdomain is made up of three β-strands: the N-terminal S1 strand (389–404, purple), the S2 strand (437–448, turquoise), and the S4 strand (473–487, blue). The RI (405–436, red dashed line) is unstructured and connects S1 and S2. In the G11a-bound structure, we observed an alternative topology (Fig. 2B) of this β-sheet where only the S2 strand is maintained in its original position. The S4 strand (blue) has unfolded to adopt a loop structure which no longer interacts with other secondary structures of NBD1. Part of the RI has become structured and interacts with the S2 strand in an antiparallel β-sheet (red) thus replacing the original S1 strand. Accordingly, the entire 389–422 segment including the canonical S1 strand, and the remainder of the RI (schematized as purple and red dashed lines in Fig. 2) is disordered in the crystal structure. As the S1 strand is replaced by a structured segment of the RI, we refer to this conformation as *β-strand-swapped (*β-SS).

Although this complex was crystallized in the presence of 2 mM ATP, we could only resolve the triphosphate of ATP with no clear density observed for the base. This observation is likely related to the fact that W401, which coordinates the adenosine base in the canonical conformation (Fig. 2C, purple), is disordered in the β-SS conformation.

In the β-SS conformation, residues 426 and 519, serving as anchor points for the FRET dyes, are separated by only 26.5 Å. Simulation of accessible dye positions using FRET-restrained positioning and screening (FPS) software[30] predicts an E_{FRET} value of 0.89 (Extended Data Figure 4 and Supplementary Table 3), which agrees remarkably well with the observed value of 0.9 (Fig. 1). We conclude that the high FRET state identified by smFRET corresponds to this G11a-bound β-SS conformation characterized by crystallography.

Functional wild type CFTR adopts the β-SS state

The extensive and unexpected structural rearrangements observed in the β-SS conformation prompted us to question its biological relevance, especially in the context of the full-length protein. As G11a binding is not compatible with the canonical conformation of NBD1, we first established whether the nanobody binds a physiologically relevant form of CFTR, an indication that the β-SS state exists naturally. To this end, we performed flow cytometry experiments on permeabilized HEK293 cells stably expressing wild-type human CFTR incubated with either nanobody G11a, nanobody T2a (a nanobody that binds a conformationally invariant epitope on NBD1[29]) or a negative control nanobody (that does not bind NBD1). We observed robust labelling of CFTR-expressing cells by nanobody G11a compared to the negative control (Fig. 3A), although signal intensity was reduced compared to T2a. This result indicates that the β-SS conformation is adopted by wild-type CFTR expressed in cells where it likely represents a subpopulation of the conformational ensemble. We also performed pull-down experiments with G11a on detergent solubilized membranes expressing wild-type CFTR. SDS-PAGE and Western blotting analysis demonstrated that G11a binds both immature and mature, fully glycosylated CFTR (Fig. 3B).

To investigate whether the β-SS conformation of NBD1 affects the function of wild-type CFTR, we studied the single-channel activity of wild-type CFTR. Figure 3D and Extended Data Figure 5 show representative recordings of an individual wild-type CFTR Cl^- channel in the absence and presence of saturating concentrations of G11a at 37 °C. Nanobody G11a binding led to an altered gating pattern of CFTR, which increased the frequency but not the duration of channel openings, leading to a 50% increase in open probability (P_o; a measure of the average fraction of time that a channel is open) (Fig. 3C). Analysis of prolonged recordings revealed that, in the presence of G11a, CFTR switched between two patterns of channel gating, one similar to wild-type and a second characterized by an elevated P_o (Extended Data Figure 5D-G). These data suggest that the alternative conformation represents an active channel state.

We conclude that nanobody G11a exclusively stabilizes a non-canonical conformation of the RI and X-ray crystallography shows that this conformation is associated with extensive structural changes in the β-subdomain of NBD1. This alternative, *β-strand-swapped* conformation is adopted by wild-type CFTR and constitutes a functional state of the channel.

The Conformational Equilibrium of NBD1 is Regulated by ATP

To characterize the conformational equilibrium of NBD1, we performed smFRET on another distance reporter. To follow the motions of the S4 strand, we labelled residues 479 and 519 which are separated by 41 Å in the canonical conformation (C_β-C_β distance), versus 35 Å in the β-strand-swapped conformation (Fig. 4A-B). Simulations of labelling these sites predict E_{FRET} values of 0.47 and 0.64, respectively (see Extended Data Figure 4B and Supplementary Table 3).

When we measured the smFRET signal of this pair (Fig. 4C), we observed two distinct states with a major population centred on E_{FRET} = 0.4 in agreement with predictions for the canonical conformation and a smaller population centred on 0.8 (larger than the value predicted from the crystal structure of the 2PT-NBD1:G11a complex). This high FRET population increased sharply in the absence of ATP (Fig. 4D), confirming that it corresponds to a non-canonical conformation. Furthermore, we observed that the data in the absence of ATP lay off the static FRET, implying dynamic behaviour on the sub-millisecond timescale. Using photon distribution analysis (PDA), we quantified the relative populations detected by FRET using 2 mM, 0.2 mM, and 0 mM ATP in the buffer (Fig. 4E). We observed that, at 2 mM ATP, about 80% of the distribution sampled the canonical state and 20% the putative β-SS conformation. The population of the canonical state was decreased to 58% and 25% for 0.2 mM and 0 mM ATP, respectively, demonstrating that modulation by ATP is concentration dependent.

We then performed a kinetic experiment where, by using 0 mM ATP, the non-canonical state was initially imposed, as evidenced by the 479-519 FRET signal at E_{FRET} = 0.8 (Fig. 4F). After 3000 s, we added ATP to a final concentration of 2 mM and observed an immediate and stable change in the FRET signal to E_{FRET} = 0.4 indicating transition to the canonical state. These data reveal that the non-canonical conformation is not an irreversible misfolded end point of the conformation landscape, but an entirely reversible state.

Subsequently, we tested the effect of G11a binding on the 479-519 reporter pair using 2 mM ATP and detected a shift of the population to E_{FRET} = 0.8 (Fig. 4G). We deduced that the high FRET state observed in the absence of the nanobody matches the opening of the S4 strand in the β-SS state captured with the G11a-NBD1 crystal. However, analysis of the FRET vs. donor lifetime 2D plot showed that this population lies on the static FRET line (Fig. 4G), indicating that binding of G11a stabilizes the opening of the S4 and restricts its dynamics.

The RI Confers Structural Plasticity on the β-subdomain

We performed the smFRET experiments with a ΔRI-2PT variant, where the regulatory insertion has been removed (405-436, red in Fig. 4A-B), and observed a single population with E_{FRET} = 0.4, matching the expected value for the canonical state (Fig. 4H).

To confirm that the RI increases plasticity of the S4 strand, we performed hydrogen deuterium exchange coupled to mass spectrometry (HDX-MS), which identifies deuterium uptake of labile protons on backbone amides to report solvent accessibility and conformational flexibility. In the presence of the RI, we observed a rapid and marked exchange of backbone amide hydrogens of the peptide 475–490, containing the S4 strand residues, indicative of increased structural flexibility (2PT-NBD1, blue; Extended Data Figure 6I). By contrast, for the ΔRI-NBD1 variant, the uptake remained limited, even after 2 h of incubation (ΔRI-NBD1, black), thus confirming that the RI enables flexibility of the S4 strand.

In the β-SS conformation, the N-terminal S1 strand is disordered and no longer interacts with the S2 and S4 strands of the β-subdomain (Fig. 2B). To probe the conformational equilibrium of the S1 strand, we used the 390-519 reporter pair and performed the same experiments as above (Extended Data Figure 6). We observed two coexisting FRET states which can be reliably attributed to the canonical and β-SS conformations by using either a ΔRI variant or the G11a nanobody, respectively. As observed with the 479-519 reporter pair, the equilibrium is regulated by the presence of ATP and is reversible. Moreover, as the same conformational profiles are observed with two different FRET pairs, we conclude that this represents the intrinsic dynamics of the protein with little or no effect of the FRET labels.

HDX-MS also demonstrated that the dynamics of this N-terminal region of NBD1 is directly coupled to the presence of the RI as we observed very limited exchange in the 392–399 peptide in ΔRI-NBD1 compared to

2PT-NBD1 (Extended Data Figure 6J). These findings are in agreement with previous HDX studies which identified the RI, the N-terminus and the S4 strand as fast-exchanging regions[31].

We conclude that two conformations of the S4 and S1 segments can be distinguished by smFRET. One corresponds to the canonical conformation where both S1 and S4 segments are engaged in the canonical β-sheet. The other is promoted by depletion of ATP and matches predictions for the β-SS conformation observed by crystallography with an unstructured S4 and a disordered S1 segment.

F508del Modulates the Conformational Equilibrium of NBD1

We then investigated the effects of the F508del mutation and other destabilizing factors on the conformational equilibrium of NBD1 (Fig. 5A illustrates regions of interest). Using the 479-519 reporter as a proxy, we observed that removing F508 did not affect the equilibrium at 22 °C (Fig. 5B and Supplementary Table 4). It is known that the effects of F508del are strongly temperature-dependent as demonstrated by robust recovery of CFTR expression and function when cells expressing F508del-CFTR are grown below 30 °C[32]. To test whether increasing the temperature altered the relative equilibrium populations, we performed smFRET measurements at 37 °C and observed a decrease in the canonical state of 2PT-479-519 when compared to the same construct at 22 °C (Fig. 5B), indicating that the conformational equilibrium is temperature-dependent.

When we probed the conformational equilibrium at 37 °C, we observed that removal of F508del decreased the population of the canonical state (Fig. 5B), indicating that the CF-causing mutation modulates the equilibrium in favour of a non-canonical state at physiological temperatures.

The 2PT-NBD1 construct used here contains 3 stabilizing substitutions: S492P, A534P and I539T which reduce the impact of F508del on the maturation of the full-length protein[15] (Fig. 5A, green). In human NBD1, Ser492 is a critical node in the allosteric network propagating thermal fluctuations between the β-subdomain and the F508 loop region[33]. To better understand the consequences of deleting F508, we analysed the impact of F508del on the PT-NBD1 construct (carrying only two stabilizing mutations: A534P and I539T), bearing S492 as in wild-type human CFTR. Using the 479-519 reporter, we observed a modest decrease in the population of the canonical state from 80% (2PT-NBD1) to 76% (PT-NBD1) at room temperature but a stronger decrease at 37 °C, from 69% to 58% (Fig. 5B). Finally, when combining the destabilizing factors to probe the F508del-PT-NBD1 variant at 37 °C, less than 40% of the population remained in the canonical state, despite the presence of 2 mM ATP (Fig. 5C). Extended Data Figure 7 details how each individual parameter gradually influences the conformational equilibrium.

We conclude that conditions that reduce the effects of F508del on the full-length CFTR protein (i.e. low temperature or stabilizing mutations) favour the canonical state in our smFRET experiments. By contrast, deletion of F508 decreases the canonical population, but only at permissive temperatures (i.e. 37 °C).

β-subdomain Unfolding Occurs in Non-Canonical States of NBD1

We surmised that the conformational plasticity of the RI and the β-subdomain plays a key role in the molecular origin of NBD1 misfolding. As we observed that the presence of the RI allows the dissociation of the S1 and S4 strands from the canonical β-sheet, we tracked domain unfolding by monitoring conformational changes in the rest of the β-sheet, specifically strand S2. Motion of this region is relevant to pathogenesis as residue K447 located in the S2 strand (Fig. 5D, turquoise) is SUMOylated in F508del-NBD1, but not in WT-NBD1[23], suggestive of increased exposure in mutant CFTR. We monitored the conformations of the S2 strand in smFRET by labelling residues 442 and 519. Importantly, residue 447 (and 442) is not involved in the structural rearrangements that occur between the canonical and β-SS states (Fig. 2B-C). At 22 °C, the smFRET signal of the 442-519 reporter pair in the context of 2PT-NBD1 showed a major static population with E_{FRET} centred on 0.4 (Fig. 5E) which agrees with the expected value based on the crystal structures (Supplementary Table 3). In addition to this low FRET state, we observed a minor diffuse population with E_{FRET} values above 0.5. This indicates the coexistence of conformations where residue 442 approaches residue 519, a condition that requires local unfolding of the S2 strand. The diffuse population disappeared entirely when the RI was absent

(Fig. 5F), suggesting that it is linked to non-canonical states. We repeated the experiment at 37 °C where 2PT-NBD1 showed a marked increase in this high E_{FRET} population (Fig. 5G).

When we measured the FRET signal of the 442-519 reporter pair at 37 °C in the PT-NBD1 variant, the proportion of high FRET population further increased compared to 2PT-NBD1 (Fig. 5H). Thus, the presence of S492, which decreased the population of canonical conformers (Fig. 5B), also favoured local unfolding of the β-sheet.

Finally, upon deletion of F508, the high FRET population increased again with fluorescence signals deviating from the static FRET line (Fig. 5I), indicative of highly dynamic behaviour. The broad distribution of E_{FRET} values from 0.5 to 1 is suggestive of a disordered state. By contrast, preincubation of the F508del-PT variant with G11a completely prevented local unfolding of the β-subdomain at 37 °C as the entire population became static with E_{FRET} = 0.4 (Fig. 5J). This matches the expected values for the β-SS conformations and agrees with the thermal stabilization of NBD1 upon binding of G11a. This suggests that binding of G11a traps NBD1 in the β-SS state and protects the β-subdomain from unfolding.

Discussion

Our data demonstrate that CFTR alternates between the state observed by cryo-EM where NBD1 adopts the canonical conformation (Fig. 6A), and one (or more) non-canonical states where NBD1 adopts a conformation which has not been observed previously (Fig. 6B). Transitions towards the latter require the RI, a unique 32-residue intrinsically disordered segment[13,34]. A *β-strand-swapped* state was trapped with nanobody G11a and resolved by crystallography, revealing dramatic topological changes whereby the RI rearranges into a β-strand with the S4 loop disengaging from the β-sheet, and the 389–422 segment becoming unstructured (Figs. 2B and 6B).

Electrophysiological measurements showed that the G11a-stabilized *β*-SS state leads to enhanced CFTR channel activity. Although more experiments are required to confirm that such an effect is solely due to conformational restriction, this conclusion is supported by experiments showing that partial deletion of the RI decreased the P_o of the channel[35].

If the *β-SS* state leads to enhanced CFTR channel activity, this alternative conformation might have evolved for functional reasons. Indeed, the high conservation of the RI in all CFTR orthologs and its absence in other ABC transporters endows a functional role specific to CFTR. Our study suggests that the RI might act as a conformational switch (i.e. between low and high channel activities).

Intrinsically disordered regions have been proposed to achieve their functions through various processes such as folding upon binding of a partner, known as “coupled folding and binding”[36], or forming dynamic, “fuzzy” complexes. Our data offer a new mechanism where function (here increased channel activity) is achieved by conferring structure on a disordered segment that replaces a structure which, in turn, needs to unfold. The changes occur within a single domain, without requiring an external molecular partner and the two states are reversible and in equilibrium. Our smFRET experiments show that ATP binding regulates this equilibrium and, although both states co-exist at saturating concentration of ATP (2 mM), transient and/or local changes in ATP concentration[37] could modulate the conformational equilibrium (and thus the activity) of CFTR. This could explain why tight ATP binding is lost in F508del-CFTR and recovered upon removal of the RI as the mutation decreases the population of the canonical conformation where W401 coordinates the adenine base of ATP.

Disordered regions are known to be hotspots for post-translational modifications which often trigger their functional activation. Of note, the RI segment contains a phosphorylation site at position S422 and its modification could therefore serve as a regulator of the conformational switch.

While the conformational plasticity conferred by the RI appears to provide functional gain, it may also bring about increased vulnerability to misfolding, especially in the presence of destabilizing mutations such as F508del. Our smFRET measurements show that conditions which are known to compensate for the effects of the pathogenic mutation *in cellulo* (such as stabilizing mutations, decreased temperatures, or removal of the

RI) are associated with stabilization of the canonical population of NBD1. This is consistent with the observation that F508del does not lead to structural changes in NBD1 constructs bearing stabilizing mutations[12]. By contrast, we observed that introducing F508del in a permissive context (37 °C, non-stabilized variant) leads to loss of the canonical conformer, which was correlated with unfolding of the β-subdomain, measured by motion of the S2 strand (Fig. 5). This state is thus distinct from the β-SS conformation where the S2 strand is well folded (Fig 5J).

We propose that, in a structurally compromised context, the reorganization of the β-subdomain which characterizes the β-SS conformation facilitates local unfolding (or prevents correct folding during biogenesis). Specifically, destabilizing factors such as F508del would ease the transition from the β-SS state to an unfolding intermediate (Fig. 6C) where the entire β-subdomain is unfolded, in agreement with the observed motion of residue 442 (Fig. 5I). As the unfolding intermediates accumulate, the canonical population is decreased (Fig. 6A-B) and transition to a fully misfolded state promoted (Fig. 6C). The idea that F508del leads to unfolding in the β-subdomain is supported by previous HDX studies of NBD1 featuring only one stabilizing mutation[31]. In these studies, removal of F508 led to substantially different exchange rates only in the region around F508 itself, the N-terminus (the S1 strand) and the S2 strand[31].

Importantly, as this unfolding pathway strictly requires the presence of the RI, this model explains why its removal is protective against F508del[21]. Likewise, it provides an explanation for protection by S492P[15] (and possibly other revertant mutations) as the mutation allosterically limits the conformational transitions proposed above.

Previous models have proposed unfolding pathways for F508del-NBD1 in the absence of the RI[6], suggesting that the destabilizing effects of the deletion affects the integrity of the canonical conformation of NBD1. Our data suggest that, in a physiological context (where the RI is present), another pathway must be considered. In this pathway, F508del primarily topples CFTR from a topologically modified conformation that was not observed previously and relies on the RI.

The discovery of a new NBD1 conformation with pathophysiological implications changes our understanding of CFTR biology. It might also open conformation-specific therapeutic approaches for F508del and possibly other related CF-causing mutations. Our study sheds new light on how structured and unstructured regions of a protein can interchange for functional reasons and might constitute a new mechanism to modulate protein function that could extend to other biological systems.

References

1. Riordan, J. R. *et al.* Identification of the cystic fibrosis gene: Cloning and characterization of complementary DNA. *Science.* **245**, 1066–1073 (1989).

2. Ratjen, F. *et al.* Cystic fibrosis. *Nat. Rev. Dis. Prim.* **1**, 15010 (2015).

3. Zhang, Z., Liu, F. & Chen, J. Molecular structure of the ATP-bound, phosphorylated human CFTR. *Proc. Natl. Acad. Sci. U. S. A.* **115**, 12757–12762 (2018).

4. Lukacs, G. L. & Verkman, A. S. CFTR: Folding, misfolding and correcting the ΔF508 conformational defect. *Trends Mol. Med.* **18**, 81–91 (2012).

5. Serohijos, A. W. R. *et al.* Phenylalanine-508 mediates a cytoplasmic-membrane domain contact in the CFTR 3D structure crucial to assembly and channel function. *Proc. Natl. Acad. Sci. U. S. A.* **105**, 3256–3261 (2008).

6. Protasevich, I. *et al.* Thermal unfolding studies show the disease causing ΔF508 mutation in CFTR thermodynamically destabilizes nucleotide-binding domain 1. *Protein Sci.* **19**, 1917–1931 (2010).

7. Wang, C. *et al.* Integrated biophysical studies implicate partial unfolding of NBD1 of CFTR in the molecular pathogenesis of F508del cystic fibrosis. *Protein Sci.* **19**, 1932–1947 (2010).

8. He, L. *et al.* Restoration of NBD1 thermal stability is necessary and sufficient to correct ΔF508 CFTR folding and assembly. *J. Mol. Biol.* **427**, 106–120 (2015).

9. Rabeh, W. M. *et al.* Correction of both NBD1 energetics and domain interface is required to restore ΔF508 CFTR folding and function. *Cell* **148**, 150–163 (2012).

10. Sharma, M., Benharouga, M., Hu, W. & Lukacs, G. L. Conformational and Temperature-sensitive Stability Defects of the ΔF508 Cystic Fibrosis Transmembrane Conductance Regulator in Post-endoplasmic Reticulum Compartments. *J. Biol. Chem.* **276**, 8942–8950 (2001).

11. Okiyoneda, T. *et al.* Peripheral protein quality control removes unfolded CFTR from the plasma membrane. *Science.* **329**, 805–810 (2010).

12. Lewis, H. A. *et al.* Impact of the ΔF508 mutation in first nucleotide-binding domain of human cystic fibrosis transmembrane conductance regulator on domain folding and structure. *J. Biol. Chem.* **280**, 1346–1353 (2005).

13. Lewis, H. A. *et al.* Structure and dynamics of NBD1 from CFTR characterized using crystallography and hydrogen/deuterium exchange mass spectrometry. *J. Mol. Biol.* **396**, 406–430 (2010).

14. Yang, Z. *et al.* Structural stability of purified human CFTR is systematically improved by mutations in nucleotide binding domain 1. *Biochim. Biophys. Acta - Biomembr.* **1860**, 1193–1204 (2018).

15. Aleksandrov, A. A. *et al.* Allosteric modulation balances thermodynamic stability and restores function of ΔF508 CFTR. *J. Mol. Biol.* **419**, 41–60 (2012).

16. deCarvalho, A. C. V., Gansheroff, L. J. & Teem, J. L. Mutations in the nucleotide binding domain 1 signature motif region rescue processing and functional defects of cystic fibrosis transmembrane conductance regulator ΔF508. *J. Biol. Chem.* **277**, 35896–35905 (2002).

17. Lewis, H. A. *et al.* Structure of nucleotide-binding domain 1 of the cystic fibrosis transmembrane conductance regulator. *EMBO J.* **23**, 282–293 (2004).

18. Atwell, S. *et al.* Structures of a minimal human CFTR first nucleotide-binding domain as a monomer, head-to-tail homodimer, and pathogenic mutant. *Protein Eng. Des. Sel.* **23**, 375–384 (2010).

19. Zhang, Z. & Chen, J. Atomic Structure of the Cystic Fibrosis Transmembrane Conductance Regulator. *Cell* **167**, 1586-1597.e9 (2016).

20. Liu, F., Zhang, Z., Csanády, L., Gadsby, D. C. & Chen, J. Molecular Structure of the Human CFTR Ion Channel. *Cell* **169**, 85-95.e8 (2017).

21. Aleksandrov, A. A. *et al.* Regulatory insertion removal restores maturation, stability and function of ΔF508 CFTR. *J. Mol. Biol.* **401**, 194–210 (2010).

22. Lukacs, G. L. *et al.* Conformational maturation of CFTR but not its mutant counterpart (ΔF508) occurs in the endoplasmic reticulum and requires ATP. *EMBO J.* **13**, 6076–6086 (1994).

23. Gong, X. *et al.* Non-native conformers of cystic fibrosis transmembrane conductance regulator NBD1 are recognized by Hsp27 and conjugated to SUMO-2 for degradation. *J. Biol. Chem.* **291**, 2004–2017 (2016).

24. Aleksandrov, L., Aleksandrov, A. A., Chang, X. B. & Riordan, J. R. The first nucleotide binding domain of cystic fibrosis transmembrane conductance regulator is a site of stable nucleotide interaction, whereas the second is a site of rapid turnover. *J. Biol. Chem.* **277**, 15419–15425 (2002).

25. Vergani, P., Lockless, S. W., Nairn, A. C. & Gadsby, D. C. CFTR channel opening by ATP-driven tight dimerization of its nucleotide-binding domains. *Nature* **433**, 876–880 (2005).

26. Cui, L. *et al.* The role of cystic fibrosis transmembrane conductance regulator phenylalanine 508 side chain in ion channel gating. *J. Physiol.* **572**, 347–358 (2006).

27. Mense, M. *et al.* In vivo phosphorylation of CFTR promotes formation of a nucleotide-binding domain heterodimer. *EMBO J.* **25**, 4728–4739 (2006).

28. Kalinin, S., Valeri, A., Antonik, M., Felekyan, S. & Seidel, C. A. M. Detection of Structural Dynamics by FRET: A Photon Distribution and Fluorescence Lifetime Analysis of Systems with Multiple States. *J. Phys. Chem. B* **114**, 7983–7995 (2010).

29. Sigoillot, M. *et al.* Domain-interface dynamics of CFTR revealed by stabilizing nanobodies. *Nat. Commun.* **10**, 2636 (2019).

30. Kalinin, S. *et al.* A toolkit and benchmark study for FRET-restrained high-precision structural modeling. *Nat. Methods* **9**, 1218–1225 (2012).

31. Premchandar, A. *et al.* New insights into interactions between the nucleotide-binding domain of CFTR and keratin 8. *Protein Sci.* **26**, 343–354 (2017).

32. Denning, G. M. *et al.* Processing of mutant cystic fibrosis transmembrane conductance regulator is temperature-sensitive. *Nature* **358**, 761–4 (1992).

33. Proctor, E. A. *et al.* Rational coupled dynamics network manipulation rescues disease-relevant mutant cystic fibrosis transmembrane conductance regulator. *Chem. Sci.* **6**, 1237–1246 (2015).

34. Kanelis, V., Hudson, R. P., Thibodeau, P. H., Thomas, P. J. & Forman-Kay, J. D. NMR evidence for differential phosphorylation-dependent interactions in WT and ΔF508 CFTR. *EMBO J.* **29**, 263–77 (2010).

35. Csanády, L., Chan, K. W., Nairn, A. C. & Gadsby, D. C. Functional roles of nonconserved structural segments in CFTR's NH_2-terminal nucleotide binding domain. *J. Gen. Physiol.* **125**, 43–55 (2005).

36. Wright, P. E. & Dyson, H. J. Intrinsically disordered proteins in cellular signalling and regulation. *Nature Reviews Molecular Cell Biology* vol. 16 18–29 (2015).

37. Ainscow, E. K., Mirshamsi, S., Tang, T., Ashford, M. L. J. & Rutter, G. A. Dynamic imaging of free cytosolic ATP concentration during fuel sensing by rat hypothalamic neurones: Evidence for ATP-independent control of ATP-sensitive K^+ channels. *J. Physiol.* **544**, 429–445 (2002).

38. Cui, L. *et al.* Domain Interdependence in the Biosynthetic Assembly of CFTR. *J. Mol. Biol.* **365**, 981–994 (2007).

39. Goddard, T. D. *et al.* UCSF ChimeraX: Meeting modern challenges in visualization and analysis. *Protein Sci.* **27**, 14–25 (2018).

Acknowledgements

We thank C.R. O'Riordan for C127 cells, John Kappes for HEK293 CFTR cells and J.R. Riordan, T. Jensen and CF Foundation Therapeutics for anti-CFTR antibodies. C.G. acknowledges support by the Fonds Forton, the Welbio (grant CR-2012S-04R), Vaincre la Mucoviscidose, Mukoviszidose e.V., the Association Luxembourgeoise de Lutte contre la Mucoviscidose, ABCF2, the Chiesi Fondation, the Cystic Fibrosis Foundation, the Fondation Air Liquide and the Fondation ULB. D.N.S acknowledges support from the CF Trust and CF Foundation Therapeutics. J.S. acknowledges support from Instruct-ERIC, part of the European Strategy Forum on Research Infrastructures (ESFRI), Instruct-ULTRA (EU H2020 Grant 731005), and the Research Foundation - Flanders (FWO) for support with nanobody discovery. C.G. is a senior Research Associate of the FRS-FNRS. D.S. was a fellow of the FRIA. We acknowledge Diamond Light Source for time on Beamlines i02, i04 and i24 under Proposals 12718 and 9426.

We are grateful to H. Remaut and B. Kobilka for careful reading of the manuscript.

We thank Frank Sobott and James Ault of the Biomolecular Mass Spectrometry department in the Astbury Centre for their support and assistance in this work, and the BBSRC (BB/M012573/1) for funding.

Author contributions

D.S., D.N.S. and C.G. conceived and designed the experiments. D.S., M.S., M.O., and R.C. performed NBD1 and nanobody expression, purification and biochemical characterization. D.S., M.S. and M.O. performed nanobody discovery, cloning and purification which E.P. and T.L. supervised. M.S. designed and conducted crystallography experiments and collected the X-ray data. M.S., C.G., A.G.P, and D.S. processed and refined the X-ray data. M.O. performed and analysed flow cytometry and CFTR pull-down experiments. Y.W. performed patch-clamp electrophysiological experiments which D.N.S. supervised. C.M. conducted the HDX-MS data collection and analysis. D.S. performed modelling, construction and labelling of FRET reporters, and smFRET experiments.

D.S., J.H. and R.C. recorded and analysed the smFRET data. D.S., D.N.S., J.S., J.H. and C.G. co-wrote the manuscript. D.N.S., J.S., J.H., and C.G. directed the study. All authors approved the final version of the manuscript.

Competing financial interests

The authors declare no competing financial interests.

Figure Legends

Fig. 1 | Single molecule FRET analysis for the 426-519 reporter pair of NBD1.

A, Depiction of the cryo-EM structure of the full-length CFTR protein (PDB: 5UAK) with its transmembrane domains (TMDs) and cytoplasmic nucleotide-binding domains (NBDs). TMD1 is coloured grey and TMD2 green. The regulatory domain and RI are unresolved. Phenylalanine-508 (F508) is shown in orange. **B**, Ribbon representation of NBD1 showing the location of the smFRET reporters in the canonical conformation (based on the published crystal structure of human NBD1, PDB: 2BBO). The positions of the labelled cysteines are shown as yellow spheres. The RI, which is not resolved in the structure, is depicted as a red dashed line. ATP and F508, located in the α-subdomain, are shown. **C-D,** FRET efficiency histograms of the 426-519 reporter in the presence and absence of 2 mM ATP and 3 mM $MgCl_2$. **E-G,** Two-dimensional plots of donor fluorescence lifetime in presence of acceptor ($\tau_{D(A)}$) versus FRET efficiency of the 426-519 reporter pair for the indicated conditions. For panel **G**, in the presence of 5 μM of nanobody G11a.

Fig. 2 | The G11a-bound structure reveals a new conformation of NBD1 with a different topology.

A, High-resolution structure of 2PT-NBD1 in complex with nanobody G11a. No density is observed for residues 389–422. **B,** and **C,** comparative representations highlighting the topological changes in the β-subdomain observed between the G11a-bound structure (**B**, the nanobody is omitted for clarity) and the canonical conformation as previously published (**C**, here PDB: 2BBO). Unresolved segments are illustrated as random coils with dashed lines in red for the RI (404–436) and in magenta for the N-terminus (389–403). The segment including the S4 strand (473–487) is coloured in blue. A topological representation of the β-subdomain is shown to the right of each conformation. In the new conformation, residues from the RI adopt a β-sheet structure and replace the S1 segment which becomes unstructured. We therefore refer to it as *β-strand-swapped*.

Fig. 3 | The G11a nanobody binds to full-length CFTR in cells and increases channel activity.

A, Flow cytometry analysis of CFTR recognition by nanobodies in CFTR overexpressing HEK293 cells. Data were normalized to the number of events acquired in each condition. Graph depicts one representative of six independent experiments. The inset shows the average median fluorescence ± SEM (fold against negative control, dashed line=1). **B,** Immunoblot of CFTR pulled down with TwinStrep-tagged nanobodies from solubilized HEK293 cells. Eluted nanobody-CFTR complexes were separated by SDS-PAGE and presence of CFTR was detected with a mouse anti-CFTR monoclonal antibody (596, recognizing residues 1204–1211 in NBD2[38]) after immunoblotting. Arrows indicate the mature (band C) and immature (band B) forms of CFTR. The blot shown is representative of 3 independent experiments. **C,** Open probabilities of wild-type CFTR in the absence and presence of G11a (1 μM). Symbols represent individual values and columns are means ± SEM (n = 6); *, P = 0.000157 vs control; Student's t-test; two-sided. **D,** Representative recordings of a wild-type CFTR Cl^- channel in an excised inside-out membrane patch from a C127 cell heterologously expressing wild-type human CFTR. The recordings were acquired at 37 °C in the presence of ATP (0.3 mM) and PKA (75 nM) in the intracellular solution. After the channel was fully activated, G11a (1 μM) was directly added to the intracellular solution bathing the membrane patch. Dotted lines indicate where the channel is closed, and downward deflections correspond to channel openings.

Fig. 4 | Single molecule FRET analysis for the 479-519 reporter pair of NBD1.

A-B, Positions of the labelled cysteines 479 and 519 for the canonical and β-SS conformations. **C-D,** Two-dimensional plots of donor fluorescence lifetime ($\tau_{D(A)}$) versus FRET efficiency for the indicated constructs and conditions. In the absence of conformational dynamics, the data clouds fall on the static FRET line (red continuous line). **E,** Overlay of FRET efficiency histograms of 2PT-479-519 for the indicated ATP concentrations. Raw data (filled) were fitted using the PDAFit software (thick lines, see Methods). Inset: Centre of the error bars shows the obtained fit for the population of the canonical conformation as calculated by PDAFit. Error bars indicate 95% confidence interval. **F,** Reversibility of the conformational change. **G-H,** Two-dimensional plot of 2PT-479-519 in presence of G11a (**G**) and of the ΔRI-2PT-NBD1 variant with 2 mM ATP (**H**).

Fig. 5 | The effects of F508del, temperature and S492P on the β-subdomain

A, Structure of the canonical conformation highlighting the positions of the 3 stabilizing mutations and F508. **B,** Histograms of the obtained fit for the population of the canonical states of the 479-519 reporter pair as calculated by PDAFit. Values are shown for 2PT-NBD1 and PT-NBD1 (with S492) variants at 22 °C and 37 °C in the presence ('F') or absence ('ΔF') of F508. Error bars indicate 95% confidence interval. **C,** Overlay of FRET efficiency histograms of 2PT-479-519 at 22 °C and F508del-PT-479-519 at 37 °C. **D,** Structure of NBD1 in the β-strand swapped conformation illustrating the positions of residues 442 and 519 (yellow spheres) along with K447 in the S2 strand (turquoise). **E-J**, Two-dimensional plots of donor fluorescence lifetime ($\tau_{D(A)}$) vs FRET efficiency of the 442-519 reporter pair for the indicated constructs and conditions.

Fig. 6 | Model of an unfolding pathway through the β-strand-swapped conformation.

Cartoon representations of the different conformational states of NBD1 superimposed onto the dephosphorylated and ATP-free full-length CFTR structure (PDB: 5UAK). **A,** The canonical conformation of human NBD1 (PDB: 2BBO) is mostly structured, only the RI (red) is unstructured. **B,** In the β-strand-swapped conformation, the N-terminus and the first half of the RI are unstructured (purple and red dashed, respectively). The second part of the RI is structured (red thick) and the S4 strand unfolds to become a loop (blue). **C,** In the unfolding intermediate, the RI and all strands of the β-sheet are unstructured (S1 in purple, RI in red, S2 in turquoise and S4 in blue). Figures of full-length CFTR structures were created using ChimeraX[39].

Methods

Human NBD1 expression and purification

Human 2PT-NBD1 (residues 387-646 containing the mutations S492P, A534P, I539T) and ΔRI-NBD1 (residues 387-646, Δ405-436) were expressed as N-terminal, His_6-SUMO fusion proteins in *Escherichia coli* (BL21 (DE3) pLysS cells) as previously described[6,17]. Cells were lysed using a French press and recombinant proteins were purified by nickel ion affinity chromatography (HisTrap HP, 1ml - GE Healthcare). The His_6-SUMO tag was removed using Ulp1 protease[40] followed by a second nickel ion chromatography. The samples were then passed through a gel filtration column (Superdex 200 Increase 10/300 GL - GE Healthcare) previously equilibrated in 20 mM Hepes pH 7.5, 150 mM NaCl, 10% (w/v) glycerol, 10% (w/v) ethylene glycol, 2 mM ATP, 3 mM $MgCl_2$, 1 mM Tris (2-carboxyethyl)phosphine (TCEP). Protein concentration was determined using Coomassie Plus (Bradford) Assay Kit (ThemoScientific).

Nanobodies discovery, cloning, expression and purification

Nanobodies against 2PT-NBD1 were obtained as previously described[29]. Briefly, a llama was immunized 6 times with purified 2PT-NBD1. Peripheral blood lymphocytes were collected after the final boost and RNA was purified to generate a phage library. Nanobodies were obtained after phage display selection, using established protocols[41]. After two rounds of selection on biotinylated 2PT-NBD1, 12 different families, classified according to the sequences of the third complementarity determining region (CDR3), were discovered. Nanobodies were cloned in pXAP100 vector encoding His_6-tag and Myc-tag at the C-terminal end of the protein. This vector was also modified to encode Twin-Strep-tag (Trp-Ser-His-Pro-Gln-Phe-Glu-Lys repeated twice with an internal linker region) instead of the His_6-tag, which was used for CFTR pull-down experiments. The expression and purification of nanobodies was performed as previously described[41]. Briefly, nanobodies were produced in *Escherichia coli* (BL21 (DE3) pLysS cells), purified from the periplasmic extract via either HisPur Ni-NTA resin (ThemoScientific) or Strep-Tactin XT Superflow resin (Iba) followed by a size exclusion chromatography (SEC) (Superdex 200 Increase 10/300 GL -GE Healthcare) into 20 mM HEPES pH 7.5, 150 mM NaCl, and 10% (w/v) glycerol.

NBD1-ELISA assay

For dose-response assays, Nunc MaxiSorp 96-well plates (ThermoScientific), were coated with 5 μg/ml NeutrAvidin Biotin-Binding protein (ThermoScientific) overnight at 4 °C and blocked for 2 h at room temperature (RT) with 4% milk in phosphate-buffered saline. Each new reagent addition was preceded by three

washes with 200 µl of NBD1 buffer (20 mM HEPES pH 7.5, 150 mM NaCl, and 10% (w/v) glycerol, 10% (w/v) ethylene glycol, 2 mM ATP, 3 mM $MgCl_2$). Then, biotinylated purified NBD1 at 5 µg/ml was immobilized for 45 min at RT followed by 1 h RT incubation with 100 µl of purified nanobody at varying concentrations (0-100 µg/ml). Signal detection was followed using His_6-tag specific antibody (0.5 µg/ml - Invitrogen) to detect the nanobodies and secondary antibody anti-mouse coupled to horse radish peroxidase (HRP) (0.5 µg/ml – Millipore). 50 µl of 1-Step UltraTMB-ELISA (ThermoScientific) served as substrate for the peroxidase and intensity of the reaction was proportional to absorbance measured at 450 nm with SynergyMx (BioTek) after addition of 50 µl H_2SO_4 at 1 M.

Thermal shift assay (DSF)

Solutions of NBD1 constructs (10 µM final concentration), nanobodies (30 µM final concentration) and 2.5x concentrated SYPRO Orange Protein Stain (Molecular Probes) diluted in NBD1 buffer, were added to the wells of 96-well PCR plates (VWR) in a final volume of 25 µl. Plates were sealed with EasySeal sheets (Molecular Dimensions) and spun for 2 min at 900 x g. SYPRO orange fluorescence was monitored in CFX96 Touch Real-Time PCR Detection System (Bio-Rad) using plate type BR white and scan mode FRET from 10 to 80 °C in increments of 1 °C.

Crystallization trials

For 2PT-NBD1:G11a complex formation, G11a nanobody was SEC purified the day before in 20 mM Hepes pH 7.5, 150 mM NaCl, 10% (w/v) glycerol and mixed with freshly SEC purified NBD1 with 1.2 molar excess of G11a, and keeping 2 mM ATP, 3 mM $MgCl_2$ and 1 mM TCEP final concentrations. Protein complex was incubated overnight on ice and then concentrated onto 30 kDa MWCO Amicon concentrator (Millipore) until protein concentration reached 11 mg/ml. Crystallization was performed in sitting drops at room temperature, adding 100 nl of protein to 100 nl of the precipitant (0.2 M $CaCl_2$, 0.1 M Tris pH 8.5, 25% (w/v) PEG 4000 and were set up immediately using a Mosquito robot (Art Robbins). Crystallization plates were incubated at 20 °C. Single crystals were mounted in CryoLoops (Molecular Dimensions Ltd) and flash-frozen in liquid nitrogen.

Crystal structure determination

Diffraction data were collected at 100 K at Proxima1 beamline of Soleil (Gif-sur-Yvette, France) synchrotron as indicated in Table S2. Data were processed using the Autoproc program[42]. The dataset was solved by molecular replacement using Molrep[43]. Subsequently, several cycles of model building, using COOT[44], combined with refinement using BUSTER 2.10.1[45] were conducted. Finally, structure validation was performed with MOLPROBITY[46]. Figures and structural comparisons of the 2PT-NBD1:G11a complex with the human NBD1 structure previously published (PDB: 2BBO[13]) were prepared using Chimera[47].

Flow cytometry

HEK293 cells stably overexpressing human wt-CFTR[48] were permeabilized with 0.01% n-Dodecyl-β-D-Maltopyranoside (β-DDM - Inalco) at least for 2 h on ice. Cells were incubated with 50 µg/ml nanobodies and DAPI (2.5 µM – Invitrogen) to monitor the permeabilization state. Nanobody binding was detected using Myc-tag specific antibody (2 µg/ml – Life Technologies) and then anti-mouse-Alexa Fluor 700 (1.3 µg/ml – Invitrogen) for 30 min on ice. We used the T2a nanobody as positive control for CFTR binding[29] and a nanobody directed against *Lactococcus lactis* multidrug resistance protein as negative control. Cells were washed once between each step by centrifugation (200 x g for 5 min at 4 °C). All incubations (100 µl) and washes (1.5 ml) were performed in PBS with 6% fetal bovine serum (FBS) and 0.01% β-DDM on ice. Cell fluorescence was measured with Gallios Flow Cytometer (Beckman Coulter). Alexa-Fluor signal (laser : 633 nm – detector : 725/20 nm) was recorded after gating on cells positive for CFTR-EGFP (laser : 488 nm – detector : 525/50 nm) and permeabilized/positive for DAPI (laser : 405 nm – detector : 450/50 nm). Gating graphs are shown in Fig S8. Data was analyzed with Kaluza software.

CFTR pull-down

Human wt-CFTR was extracted from HEK293 cell pellets by solubilization with 0.1% DMNG in PBS with protease inhibitors for 1 h at 4 °C. The cell debris was removed by centrifugation (16,000 x g for 30 min at 4 °C). Supernatant was diluted 10 times in PBS with protease inhibitors and incubated for 30 min on 10 µl Strep-Tactin XT Superflow resin (Iba) pre-loaded with 200 µg nanobodies. Resin was washed and eluted with Buffer BXT (Iba). The presence of CFTR in each sample was detected by SDS-PAGE and immuno-blotting.

SDS-PAGE and immunoblotting

Cell extracts were separated by SDS-PAGE on 7.5% polyacrylamide gels and transferred to nitrocellulose membranes (Bio-Rad) for immunodetection. After blocking for 1 h with 5% bovine serum albumin (BSA) in Tris-buffered saline added Tween-20 (TBST), CFTR was detected using monoclonal antibody 596[38] for 1 h in blocking buffer. Blots were washed 3 times for 5 min and incubated with anti-mouse-HRP antibody (0.2 µg/ml – Millipore) for 1 h in TBST. Membranes were washed 3 times for 5 min. CFTR was visualized by chemiluminescence using Luminata Forte Western HRP Substrate (Millipore) and detected with ImageQuant 400 (GE Healthcare).

Single-channel studies

For patch-clamp experiments, we used mouse mammary epithelial (C127) cells stably expressing wild-type human CFTR (gift of C. R. O'Riordan (Sanofi Genzyme)). They were cultured and used as described previously[49].

CFTR Cl^- channels were recorded in excised inside-out membrane patches using an Axopatch 200B patch-clamp amplifier and pCLAMP software (version 10.4) both from Molecular Devices (San Jose, CA, USA) as described previously[49]. The pipette (extracellular) solution contained (mM): 140 N-methyl-D-glucamine, 140 aspartic acid, 5 $CaCl_2$, 2 $MgSO_4$ and 10 N-tris[hydroxymethyl]methyl-2-aminoethanesulphonic acid (TES), adjusted to pH 7.3 with Tris ($[Cl^-]$, 10 mM). The bath (intracellular) solution contained (mM): 140 NMDG, 3 $MgCl_2$, 1 CsEGTA and 10 TES, adjusted to pH 7.3 with HCl ($[Cl^-]$, 147 mM; free $[Ca^{2+}]$, < 10^{-8} M) and was maintained at 37 °C.

CFTR Cl^- channels were activated promptly following membrane patch excision and clamping voltage at –50 mV using the catalytic subunit of protein kinase A (PKA (purified from bovine heart); 75 nM) and ATP (1 mM), both from Merck Life Science UK Ltd.. To test the effects of nanobodies on wild-type CFTR, we added them to the intracellular solution and acquiring 5 – 10 minutes of single-channel data in the continuous presence of ATP (0.3 mM) and PKA (75 nM). Because of the difficulty of removing nanobodies from the recording chamber, specific interventions were compared with the pre-intervention control period made with the same concentration of ATP and PKA, but without nanobodies. To minimise rundown, PKA and ATP were added to all intracellular solutions. On completion of experiments, the recording chamber was thoroughly cleaned before re-use.

In this study, we used excised inside-out membrane patches containing ≤ 5 active channels, determined using the maximum number of simultaneous channel openings observed during an experiment[50]. After recording, filtering and digitizing data[51], single-channel current amplitude (i), open probability (P_o), mean burst duration (MBD) and interburst interval (IBI) were determined as described previously[50,51]. Results are expressed as means ± SEM of n observations, where n represents the number of individual membrane patches obtained from different cells. Using SigmaPlot™ (version 13.0, Systat Software Inc., San Jose, CA, USA), we tested for differences between two groups of data acquired within the same experiment with Student's t-test. Differences were considered statistically significant when $P < 0.05$.

Hydrogen deuterium exchange mass spectrometry

Experiments

Hydrogen deuterium exchange mass spectrometry (HDX-MS) experiments were performed on a Synapt G2Si HDMS coupled to an Acquity UPLC M-Class system with HDX and automation (Waters Corporation, Manchester

UK). Protein samples were used at a concentration of 50 µM. Isotope labelling was initiated by diluting 5 µl of each protein sample into 95 µl of buffer L (HEPES 20 mM pD 7.5, NaCl 100 mM) complemented with 2 mM ATP, 3 mM $MgCl_2$ when specified. The protein was incubated for 1, 5, 30, and 120 min to capture a range of exchange times and then quenched in buffer Q (100 mM potassium phosphate, brought to pH 2.3 with formic acid) at 4 °C before being digested on-line with a Waters Enzymate BEH pepsin column at 20 °C, for ~30 s, at a pressure of ~2000 psi. The same procedure was used for undeuterated controls, with the labelling buffer being replaced by buffer E (HEPES 20 mM pH 7.5, NaCl 100 mM). The peptides were trapped on a Waters BEH C18 VanGuard pre-column for 3 min at a flow rate of 200 µl/min in buffer A (0.1% formic acid ~ pH 2.5) for desalting before being applied to a Waters BEH C-18 analytical column. Peptides were eluted with a linear gradient of buffer B (8-40% gradient of 0.1% formic acid in acetonitrile) at a flow rate of 40 µl / min. All trapping and chromatography steps were performed at 1 °C to minimize back exchange. The electrospray ionization source was operated in the positive ion mode and ion mobility was enabled for the MS instrument. $HDMS^E$ data were acquired with a 20 to 30 V trap collision energy ramp for high-energy acquisition of product ions. Optimized peptide identification and peptide coverage for all samples was performed from undeuterated controls (five replicates). All deuterium time points were performed in triplicate. Leucine Enkephalin (LeuEnk - Sigma) was used as a lock mass for mass accuracy correction and the MS was calibrated with sodium iodide. The on-line Enzymate pepsin column was washed between each injection with pepsin wash (1.5 M Gu-HCl, 4% MeOH, 0.8% formic acid) recommended by the manufacturer to prevent significant peptide carry-over from the pepsin column and a blank run was performed between each technical triplicate. Measurements were performed on three biological replicates.

Data evaluation and statistical analysis

Sequence identification was made from MS^E data from the undeuterated samples using ProteinLynx Global Server 2.5.1 (PLGS Waters Corp. Manchester UK). The output peptides were filtered using DynamX (v. 3.0) using the following filtering parameters: minimum intensity of 1000, minimum and maximum peptide sequence length of 5 and 25 respectively, minimum MS/MS products of 2, minimum products per amino acid of 0.28, minimum score of 5, and a maximum MH^+ error threshold of 15 ppm. The peptides had to be identified in 3 out of 5 replicates. Additionally, all the spectra were visually examined and only those with high signal to noise ratios were used for HDX-MS analysis. The amount of relative deuterium uptake for each peptide was determined using DynamX (v. 3.0) and were not corrected for back exchange since only relative differences were used for analysis and interpretation and there was no benefit from normalizing the data[52]. The relative fractional uptake (RFU) was calculated from $RFU_a = [Y_{a,t}/ (MaxUptake_a \times D)]$, where *Y* is the deuterium uptake for peptide *a* at incubation time *t*, and *D* is the percentage of deuterium in the sample after mixing the protein with the labeling solution. 99% Confidence intervals were calculated using Deuteros[53] and were found to be of 0.7 Da or smaller for the sum of RFU over all time points.

Modeling of dye distributions using the FPS simulation program

We used the FRET-restrained positioning and screening (FPS) software[30] to calculate accessible volumes and theoretical approximations of distances and FRET efficiencies between fluorophores fixed onto cysteines in key regions of NBD1.

Site-directed mutagenesis for the generation of single molecule PIE-FRET constructs

Guided by previous studies of functional full-length cysteine-less CFTR variants[26,27], we replaced endogenous cysteines of 2PT-NBD1. Cysteines 491 and 524 were converted to alanine and cysteines 590 and 592 to valine. Substitutions were done by the QuikChange™ site-directed mutagenesis procedure using a modified protocol for primer design[54].

NBD1 fluorophore labeling

For smFRET experiments engineered cysteines of NBD1 constructs were labeled with ATTO488 and Alexa647 maleimide dyes (ATTO-TEC GmbH AD 488-41 and ThermoFisher A20347, respectively). Affinity-purified NBD1 at 70 µM in labeling buffer (20 mM HEPES pH 7.20-7.40, 150 mM NaCl, 10% (w/v) glycerol, 10% (w/v) ethylene glycol 2 mM ATP, 3 mM $MgCl_2$ and 1 mM TCEP) was incubated with a 3 times molar excess of each dye to NBD1 for a total of 3 h. Labeled NBD1 was spun at 4 °C and 16,000 g for 30 minutes and passed through a gel filtration column (Superdex 200 Increase 10/300 GL - GE Healthcare) previously equilibrated in 20 mM HEPES pH 7.5, 150 mM NaCl, 10% (w/V) glycerol, 10% (w/V) ethylene glycol, 2 mM ATP, 3 mM $MgCl_2$.

Single-molecule FRET data recording

Protein at 5-15 µM was diluted 1000-fold into the buffer (20 mM HEPES, pH 7.5, 150 mM NaCl) prior to mixing with other reagents. Then the protein was diluted 100-fold in the final measurement sample containing also 0.1 mg/mL BSA, MgATP and/or nanobody, reaching a final concentration of 50-150 pM. The BSA-coated (1 mg/ml BSA) coverslip (Nunc Lab-Tek Chambered Coverglass, Thermo Fisher Scientific) was rinsed two times with the sample solution (30 µl), prior to depositing a 30 µl drop of the same solution. Background or scatter samples were prepared similarly but without protein.

Per sample, 1-3 hour datasets were recorded at 22 °C on a homebuilt multiparameter fluorescence detection microscope with pulsed interleaved excitation (MFD-PIE) as established[55], with minor modifications. Emission from a pulsed 483-nm laser diode (LDH-P-C-470, PicoQuant) was cleaned up (Chroma ET485/20x, F49-482; AHF analysentechnik AG), emission from a 635-nm laser diode (LDH-P-C-635B, PicoQuant) was cleaned up (Chroma z635/10x, PicoQuant), and both lasers were alternated at 26.67 MHz (PDL 828 Sepia II, PicoQuant), delayed ~18 ns with respect to each other, and combined with a 483-nm reflecting dichroic mirror in a single-mode optical fiber (coupler, 60FC-4- RGBV11-47; fiber, PMC-400Si-2.6-NA012-3-APC-150-P, Schäfter + Kirchhoff GmbH). After collimation (60FC-L-4-RGBV11-47, SuK GmbH), the linear polarization was cleaned up (CODIXX VIS-600-BC-W01, F22-601; AHF analysentechnik AG), and the light (75 µW of 483-nm light and 50 µW of 635-nm light) was reflected into the back port of the microscope (IX70, Olympus Belgium NV) and upward [3-mm-thick full-reflective Ag mirror, F21-005 (AHF) mounted in a total internal reflection fluorescence filter cube for BX2/IX2, F91-960; AHF analysentechnik AG] to the objective (UPLSAPO-60XW, Olympus). Sample emission was transmitted through a 3-mm-thick excitation polychroic mirror (Chroma zt470-488/640rpc, F58-PQ08; AHF analysentechnik AG), focused through a 75-mm pinhole (P75S, Thorlabs) with an achromatic lens (AC254-200-A-ML, Thorlabs), collimated again (AC254-50-A-ML, Thorlabs), and spectrally split (Chroma T560lpxr, F48-559; AHF analysentechnik AG). The blue range was filtered (Chroma ET525/50m, F47-525, AHF analysentechnik AG), and polarization was split (PBS251, Thorlabs). The red range was also filtered (Chroma ET705/100m, AHF analysentechnik AG), and polarization was split (PBS252, Thorlabs). Photons were detected on four avalanche photodiodes (PerkinElmer or EG&G SPCM-AQR12/14, or Laser Components COUNT BLUE), which were connected to a time-correlated single-photon counting (TCSPC) device (SPC-630, Becker & Hickl GmbH) over a router (HRT-82, Becker & Hickl) and power supply (DSN 102, PicoQuant). Signals were stored in 12-bit first-in-first-out (FIFO) files. Microscope alignment was carried out using fluorescence correlation spectroscopy (FCS) on freely diffusing ATTO 488-CA and ATTO 655-CA (ATTO-TEC) and by connecting the detectors to a hardware correlator (ALV-5000/EPP) over a power splitter (PSM50/51, PicoQuant) for alignment by real-time FCS. Instrument response functions (IRFs) were recorded one detector at-a-time in a solution of ATTO 488-CA or ATTO 655-CA in near-saturated centrifuged potassium iodide at a 25-kHz average count rate for a total of 25×10^6 photons. Macrotime-dependent microtime shifting was corrected for two (blue/parallel and red/perpendicular) of four avalanche photodiodes (APDs) using the IRF data as input.

Single-molecule MFD-PIE-FRET data analysis

Data were analyzed with the PAM software[56] via standard procedures for MFD-PIE smFRET burst analysis[57,58]. Signals from each TCSPC routing channel (corresponding to the individual detectors) were divided in time gates to discern 483-nm excited FRET photons from 635-nm excited acceptor photons. A two-color MFD all-photon

burst search algorithm using a 500-µs sliding time window (minimum of 100 photons per burst, minimum of 5 photons per time window) was used to identify single donor- and/or acceptor–labeled molecules in the fluorescence traces. Double labelled single molecules were selected from the raw burst data using a kernel density estimator (ALEX-2CDE < 12)[59], that also excluded other artefacts. Sparse slow-diffusing aggregates were removed from the data by excluding bursts exhibiting a burst duration > 20 ms. By generating histograms of *E* versus measurement time, we corroborated that the distribution of *E* was invariant over the duration of the measurement. Data was corrected in this order to obtain the absolute stoichiometry parameter S and absolute FRET efficiency E: background subtraction, donor emission crosstalk correction, acceptor direct excitation correction and relative detection efficiency correction. The last value depends on the used dye combination, but also on the used detectors. By making histograms of E versus measurement time, we corroborated that the distribution of E was invariant over the duration of the measurement.

Photon distribution analysis (PDA)

Static PDA was carried out to obtain the absolute interdye distance distribution assuming two Gaussian distributed states[60]. For each FRET data set, raw bursts were re-binned in 1 ms time bins, and histograms were constructed and analyzed. Binned data was plotted in a raw (uncorrected) FRET efficiency (E_{PR}) versus uncorrected stoichiometry (S_{PR}) plot and only bins with $0.2 < S_{PR} < 0.6$ were included in the analysis to remove burst sections containing complex acceptor photophysics or photobleaching. Furthermore, only bins with at least 20 and maximally 200 photons (to reduce calculation time) were used for PDA analysis. A two-state model for a Gaussian distance distribution was used to generate a library of simulated E_{FRET} values, which was fitted to the experimental E_{FRET} histogram using a reduced χ^2–guided simplex search algorithm to obtain the amplitude, mean distance *R* and width σ of all Gaussian distributed substates and, in the case of multiple states, their area fraction *A* (%). A probability density function (PDF) was calculated per state using the R and σ parameters that describe the underlying Gaussian distributed states. The summed PDF was scaled to a total area of unity, with the PDF area of each state scaled to the corresponding fraction of molecules. A Jacobian was used to estimate confidence intervals (95%) of the fit parameters. Criteria for a good fit were a low reduced $\chi 2$ value, as well as a weighted-residual plot free of trends.

Data availability

Data supporting the findings of this manuscript are available from the corresponding author upon reasonable request. The atomic coordinates and structure factors reported in this paper have been deposited in the Protein Data Bank (PDB). The accession numbers for the structure reported in this paper is PDB: 6ZE1. The source data underlying Figs. 1-5 and Extended Data Figures 2, 3, 6 and 7 will be provided as Source Data files.

References

40. Li, S. J. & Hochstrasser, M. A new protease required for cell-cycle progression in yeast. *Nature* **398**, 246–251 (1999).

41. Pardon, E. *et al.* A general protocol for the generation of Nanobodies for structural biology. *Nat. Protoc.* **9**, 674–693 (2014).

42. Vonrhein, C. *et al.* Data processing and analysis with the autoPROC toolbox. *Acta Crystallogr. Sect. D Biol. Crystallogr.* **67**, 293–302 (2011).

43. Vagin, A. & Teplyakov, A. *MOLREP* : an Automated Program for Molecular Replacement. *J. Appl. Crystallogr.* **30**, 1022–1025 (1997).

44. Emsley, P., Lohkamp, B., Scott, W. G. & Cowtan, K. Features and development of Coot. *Acta Crystallogr. Sect. D Biol. Crystallogr.* **66**, 486–501 (2010).

45. Bricogne, G. *et al.* Bricogne, BUSTER version 2.10.1,. *Cambridge, United Kingdom: Global Phasing Ltd.* (2017).

46. Chen, V. B. *et al.* MolProbity: All-atom structure validation for macromolecular crystallography. *Acta Crystallogr.*

Sect. D Biol. Crystallogr. **66**, 12–21 (2010).

47. Pettersen, E. F. *et al.* UCSF Chimera--a visualization system for exploratory research and analysis. *J. Comput. Chem.* **25**, 1605–1612 (2004).

48. Hildebrandt, E. *et al.* A Stable Human-Cell System Overexpressing Cystic Fibrosis Transmembrane Conductance Regulator Recombinant Protein at the Cell Surface. *Mol. Biotechnol.* **57**, 391–405 (2015).

49. Sheppard, D. N. & Robinson, K. A. Mechanism of glibenclamide inhibition of cystic fibrosis transmembrane conductance regulator Cl^- channels expressed in a murine cell line. *J. Physiol.* **503**, 333–346 (1997).

50. Cai, Z., Taddei, A. & Sheppard, D. N. Differential sensitivity of the Cystic Fibrosis (CF)-associated mutants G551D and G1349D to potentiators of the cystic fibrosis transmembrane conductance regulator (CFTR) Cl^- channel. *J. Biol. Chem.* **281**, 1970–1977 (2006).

51. Rodrat, M. *et al*. Carbon monoxide-releasing molecules inhibit the cystic fibrosis transmembrane conductance regulator Cl^- channel. *Am J Physiol Lung Cell Mol Physiol*. **319**, L997-L1009 (2020).

52. Wales, T. E., Eggertson, M. J. & Engen, J. R. Considerations in the Analysis of Hydrogen Exchange Mass Spectrometry Data. in *Mass Spectrometry Data Analysis in Proteomics* (ed. Matthiesen, R.) 263–288 (Humana Press, 2013). doi:10.1007/978-1-62703-392-3_11.

53. Lau, A. M. C., Ahdash, Z., Martens, C. & Politis, A. Deuteros: Software for rapid analysis and visualization of data from differential hydrogen deuterium exchange-mass spectrometry. *Bioinformatics* **35**, 3171–3173 (2019).

54. Liu, H. & Naismith, J. H. An efficient one-step site-directed deletion, insertion, single and multiple-site plasmid mutagenesis protocol. *BMC Biotechnol.* **8**, 91 (2008).

55. Talavera, A. *et al.* Phosphorylation decelerates conformational dynamics in bacterial translation elongation factors. *Sci. Adv.* **4**, (2018).

56. Schrimpf, W., Barth, A., Hendrix, J. & Lamb, D. C. PAM: A Framework for Integrated Analysis of Imaging, Single-Molecule, and Ensemble Fluorescence Data. *Biophys. J.* **114**, 1518–1528 (2018).

57. Hellenkamp, B. *et al.* Precision and accuracy of single-molecule FRET measurements—a multi-laboratory benchmark study. *Nat. Methods* **15**, 669–676 (2018).

58. Kudryavtsev, V. *et al.* Combining MFD and PIE for accurate single-pair förster resonance energy transfer measurements. *ChemPhysChem* **13**, 1060–1078 (2012).

59. Tomov, T. E. *et al.* Disentangling subpopulations in single-molecule FRET and ALEX experiments with photon distribution analysis. *Biophys. J.* **102**, 1163–1173 (2012).

60. Antonik, M., Felekyan, S., Gaiduk, A. & Seidel, C. A. M. Separating structural heterogeneities from stochastic variations in fluorescence resonance energy transfer distributions via photon distribution analysis. *J. Phys. Chem. B* **110**, 6970–6978 (2006).

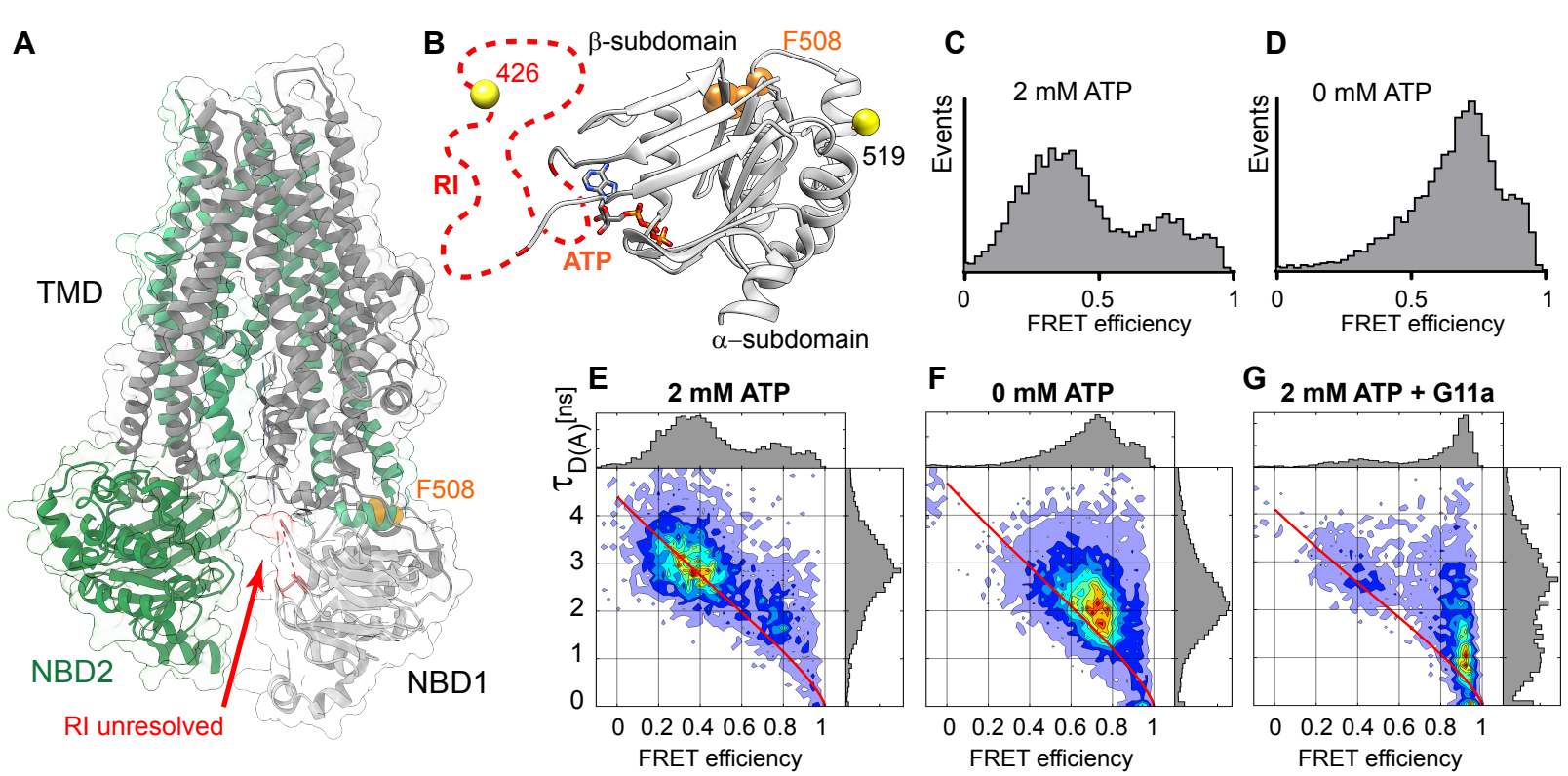
A
TMD
F508
NBD2
NBD1
RI unresolved
B
β-subdomain
F508
426
519
RI
ATP
α–subdomain
C
2 mM ATP
Events
0
0.5
1
FRET efficiency
D
0 mM ATP
Events
0
0.5
1
FRET efficiency

E
2 mM ATP
τD(A) [ns]
0
1
2
3
4
0 0.2 0.4 0.6 0.8 1
FRET efficiency
F
0 mM ATP
0 0.2 0.4 0.6 0.8 1
FRET efficiency
G
2 mM ATP + G11a
0 0.2 0.4 0.6 0.8 1
FRET efficiency

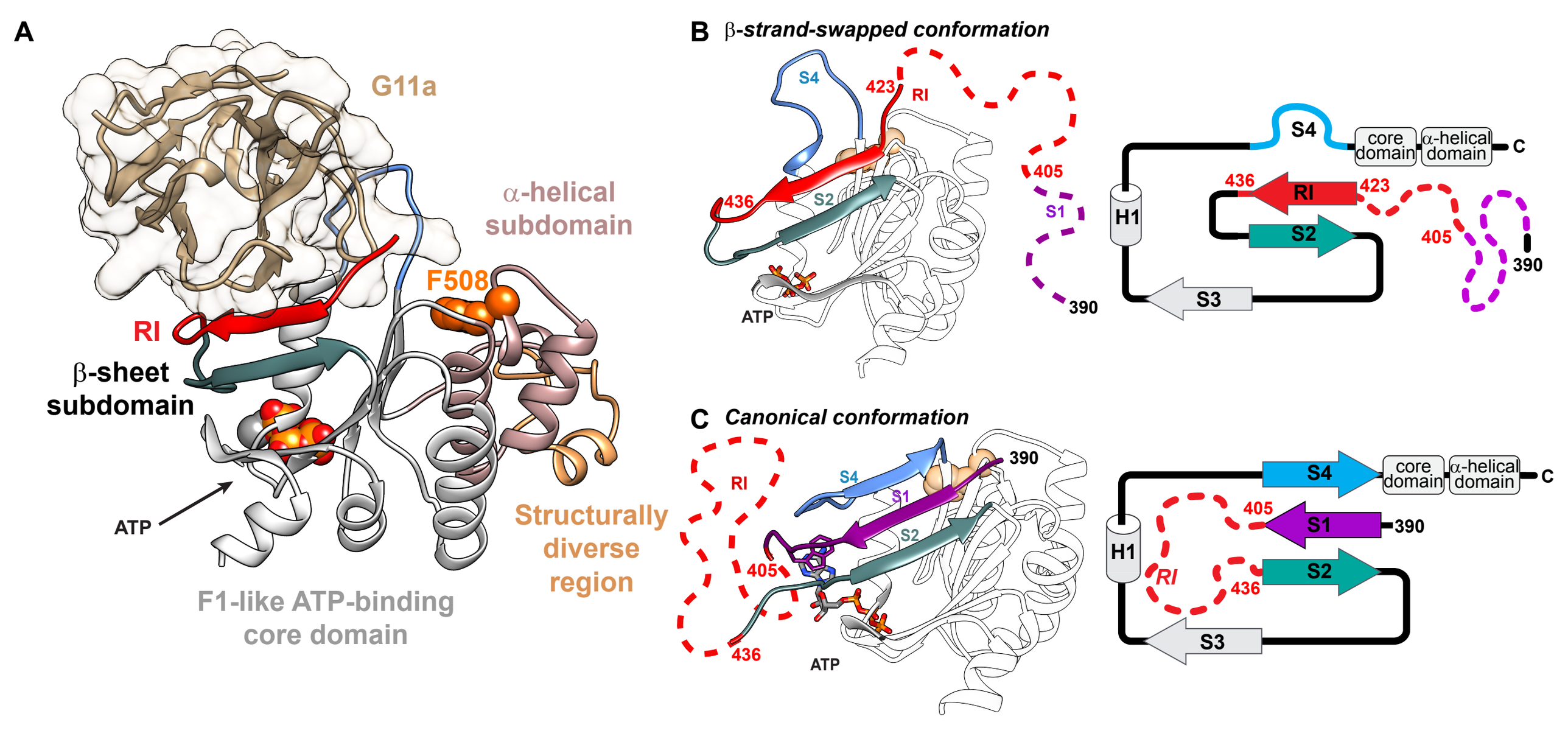
A
G11a
α-helical subdomain
F508
RI
β-sheet subdomain
ATP
Structurally diverse region
F1-like ATP-binding core domain
B β-strand-swapped conformation
S4
423
RI
436
S2
405
S1
390
ATP
S4
core domain
α-helical domain
C
436
RI
423
H1
S2
405
390
S3
C Canonical conformation
RI
S4
390
S1
S2
405
436
ATP
S4
core domain
α-helical domain
C
405
S1
390
H1
RI
436
S2
S3

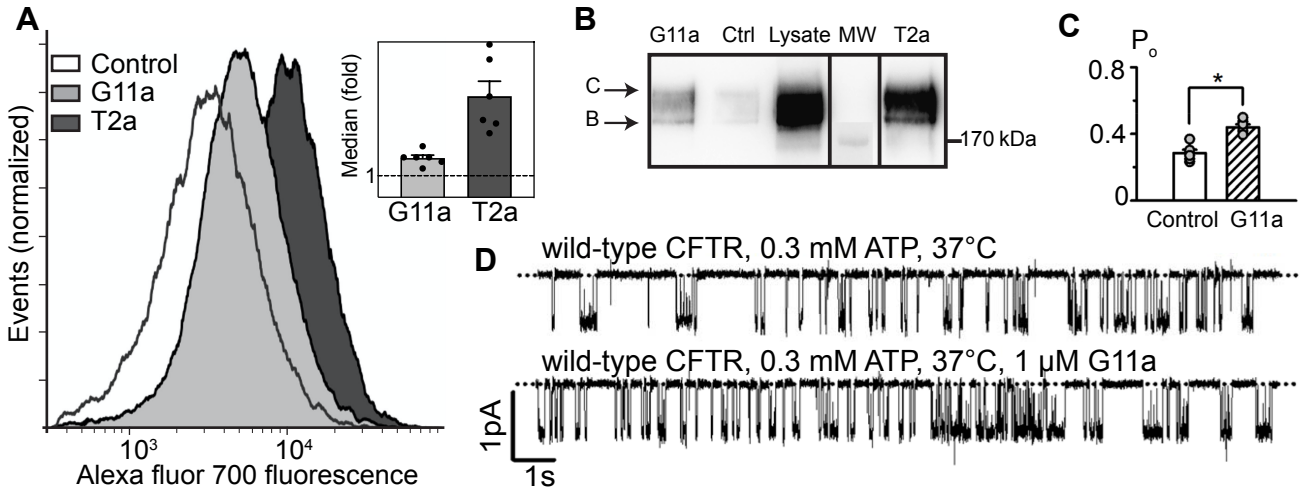
A
Control
G11a
T2a
Events (normalized)
Median (fold)
1
G11a
T2a
10^3
10^4
Alexa fluor 700 fluorescence
B
G11a
Ctrl
Lysate
MW
T2a
C
B
170 kDa
C
P_o
0.8
0.4
0
*
Control
G11a
D
wild-type CFTR, 0.3 mM ATP, 37°C
wild-type CFTR, 0.3 mM ATP, 37°C, 1 μM G11a
1pA
1s

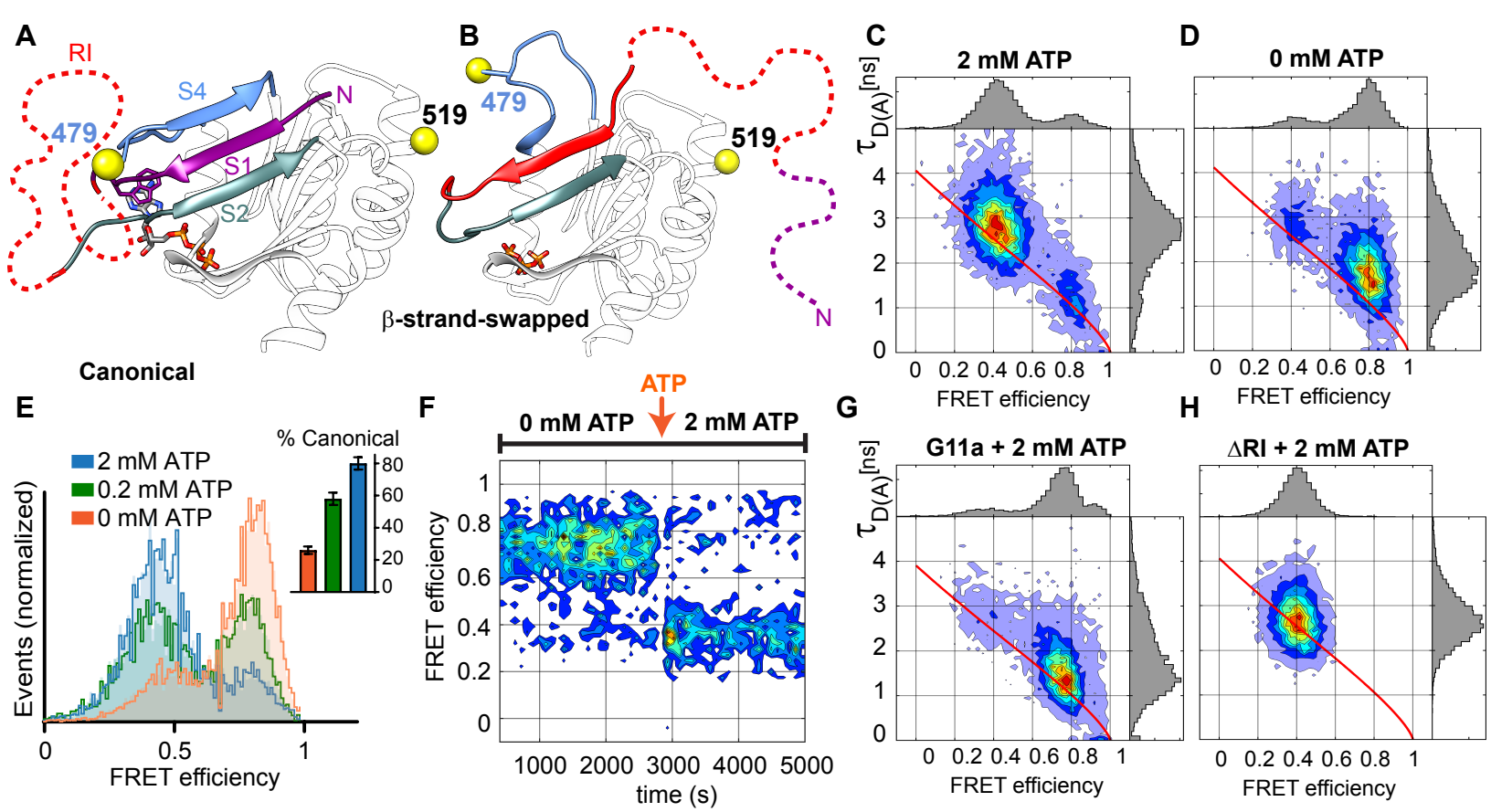
A
RI
S4
N
479
519
S1
S2
Canonical
B
479
519
N
β-strand-swapped
C
2 mM ATP
$\tau_{D(A)}$ [ns]
FRET efficiency
D
0 mM ATP
FRET efficiency

E
2 mM ATP
0.2 mM ATP
0 mM ATP
% Canonical
Events (normalized)
FRET efficiency

F
ATP
0 mM ATP
2 mM ATP
FRET efficiency
time (s)

G
G11a + 2 mM ATP
$\tau_{D(A)}$ [ns]
FRET efficiency
H
ΔRI + 2 mM ATP
FRET efficiency

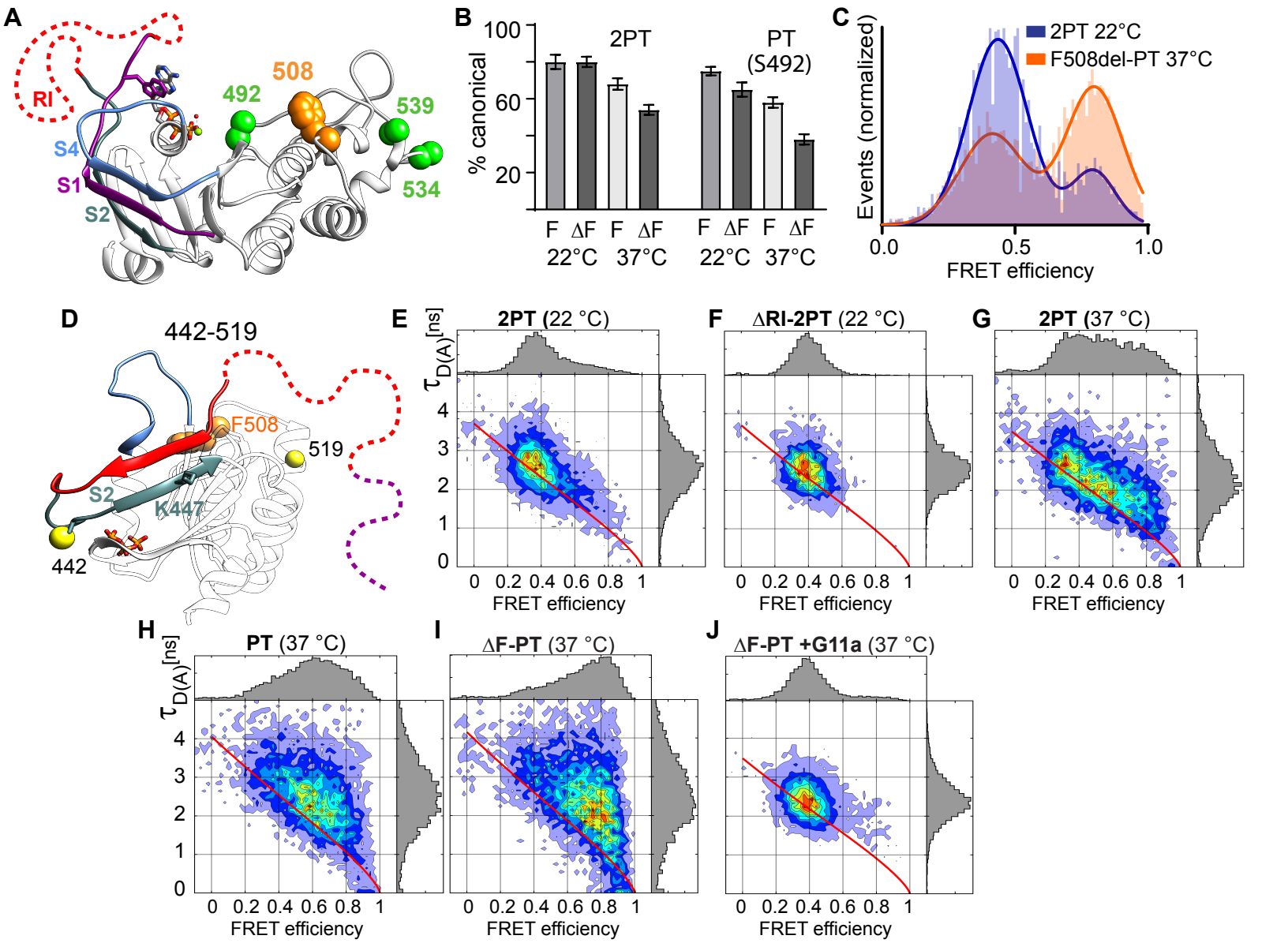
A
RI
S4
S1
S2
492
508
539
534
B
% canonical
100
60
20
2PT
PT (S492)
F ΔF F ΔF F ΔF F ΔF
22°C 37°C 22°C 37°C
C
Events (normalized)
2PT 22°C
F508del-PT 37°C
0.0
0.5
1.0
FRET efficiency
D
442-519
F508
519
S2
K447
442
E
2PT (22 °C)
F
ΔRI-2PT (22 °C)
G
2PT (37 °C)
τD(A) [ns]
0 1 2 3 4
0 0.2 0.4 0.6 0.8 1
FRET efficiency
H
PT (37 °C)
I
ΔF-PT (37 °C)
J
ΔF-PT +G11a (37 °C)

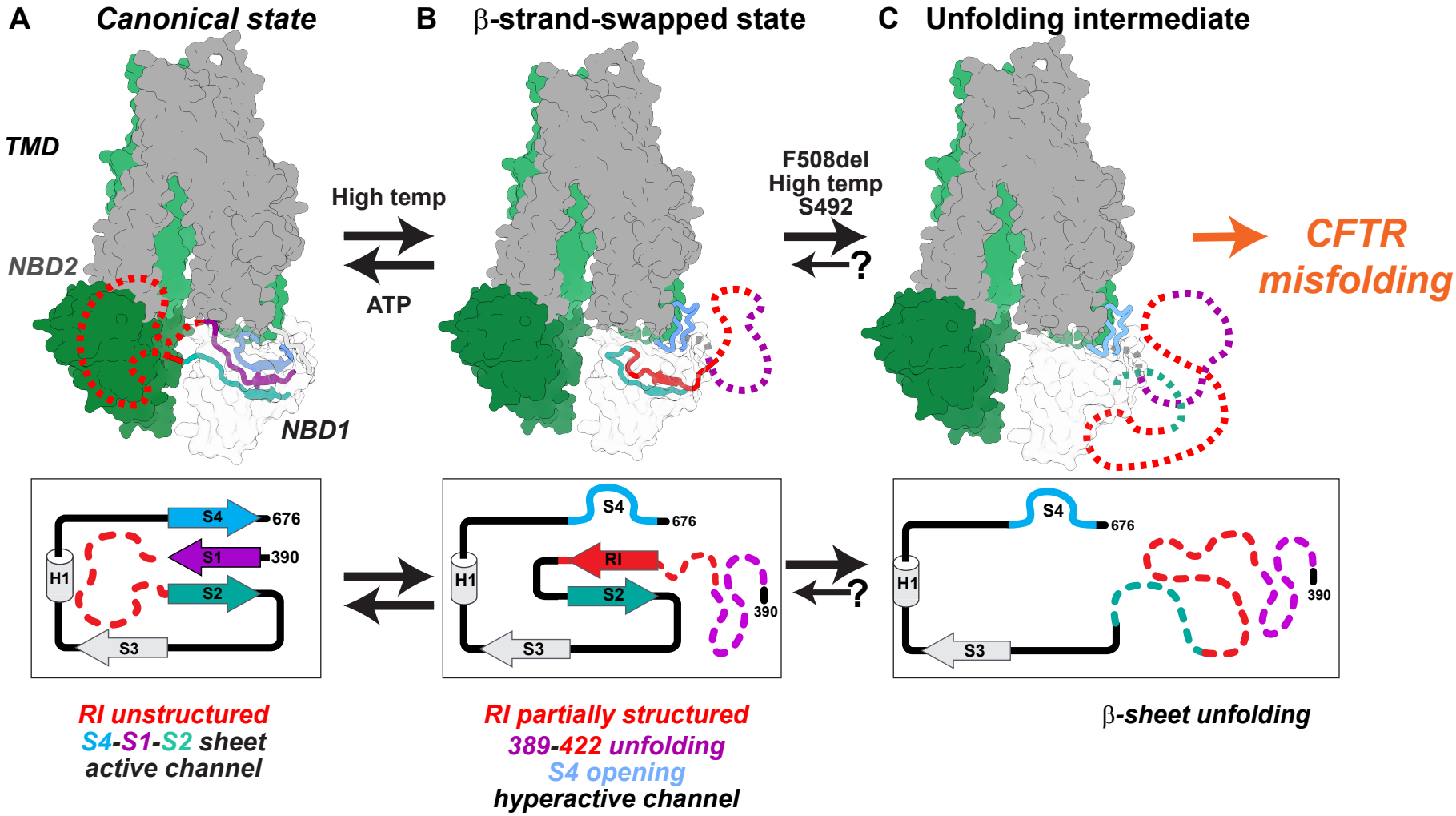
A
Canonical state
B
β-strand-swapped state
C
Unfolding intermediate
TMD
NBD2
NBD1
High temp
ATP
F508del
High temp
S492
?
CFTR
misfolding
S4
676
S1
390
S2
S3
H1
RI
?
RI unstructured
S4-S1-S2 sheet
active channel
RI partially structured
389-422 unfolding
S4 opening
hyperactive channel
β-sheet unfolding

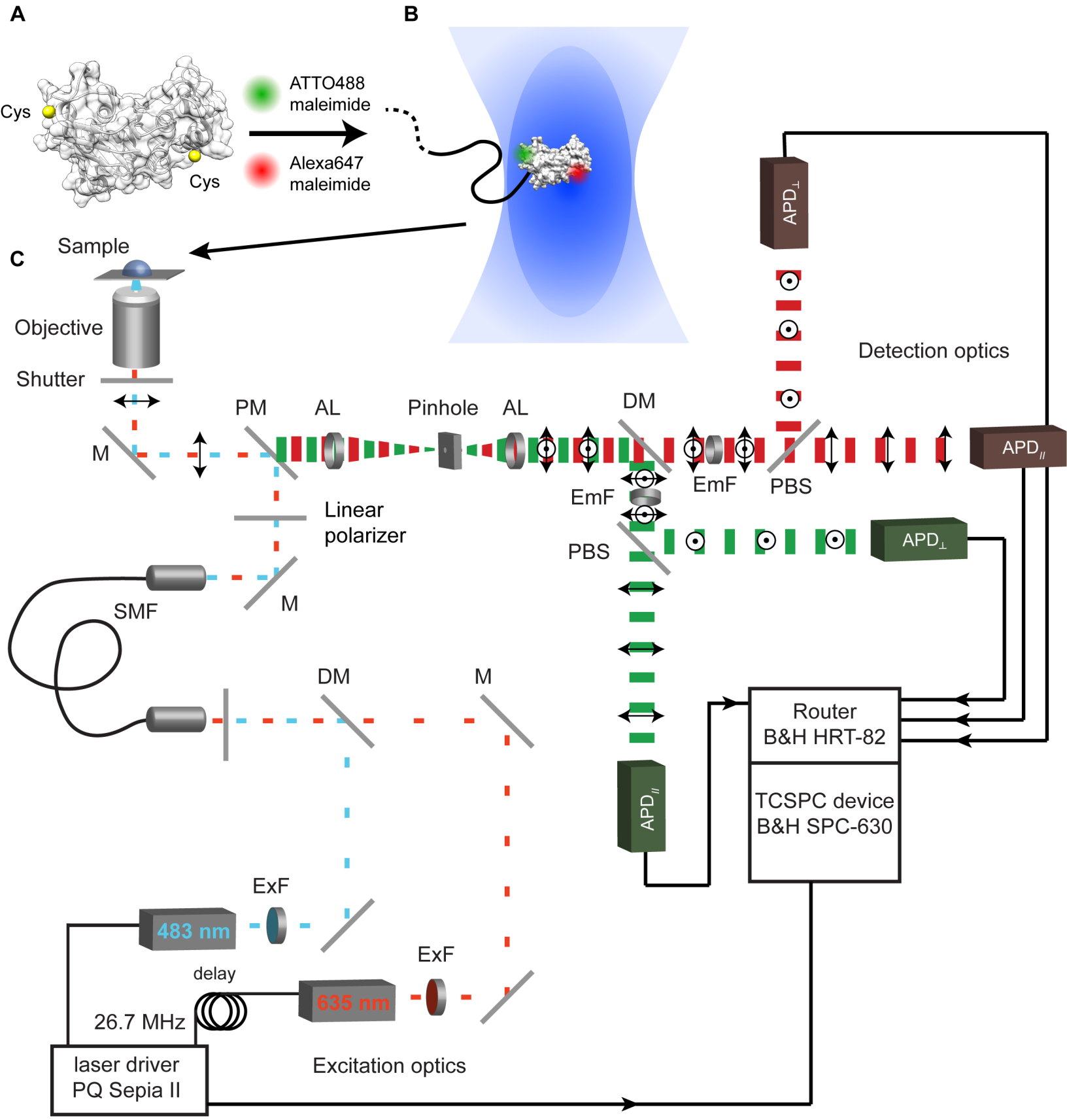
A
B
C
Cys
Cys
ATTO488
maleimide
Alexa647
maleimide
Sample
Objective
Shutter
M
PM
AL
Pinhole
AL
DM
EmF
EmF
PBS
PBS
APD⊥
APD//
APD⊥
APD//
Detection optics
Linear
polarizer
SMF
M
DM
M
ExF
ExF
483 nm
635 nm
delay
26.7 MHz
laser driver
PQ Sepia II
Excitation optics
Router
B&H HRT-82
TCSPC device
B&H SPC-630

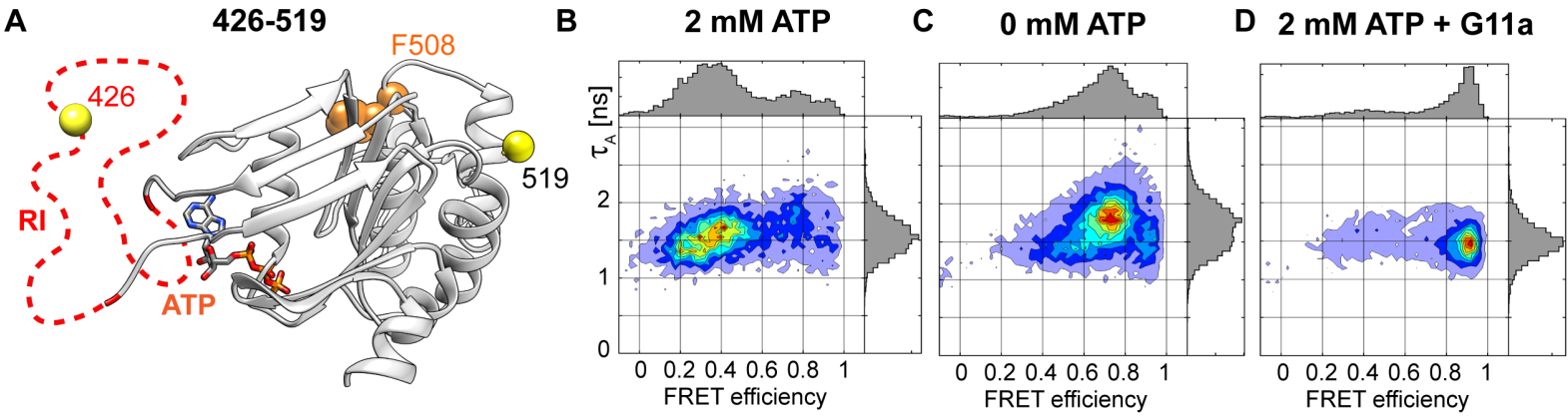
A
426-519
F508
426
519
RI
ATP
B
2 mM ATP
C
0 mM ATP
D
2 mM ATP + G11a
τA [ns]
0
1
2
0 0.2 0.4 0.6 0.8 1
FRET efficiency

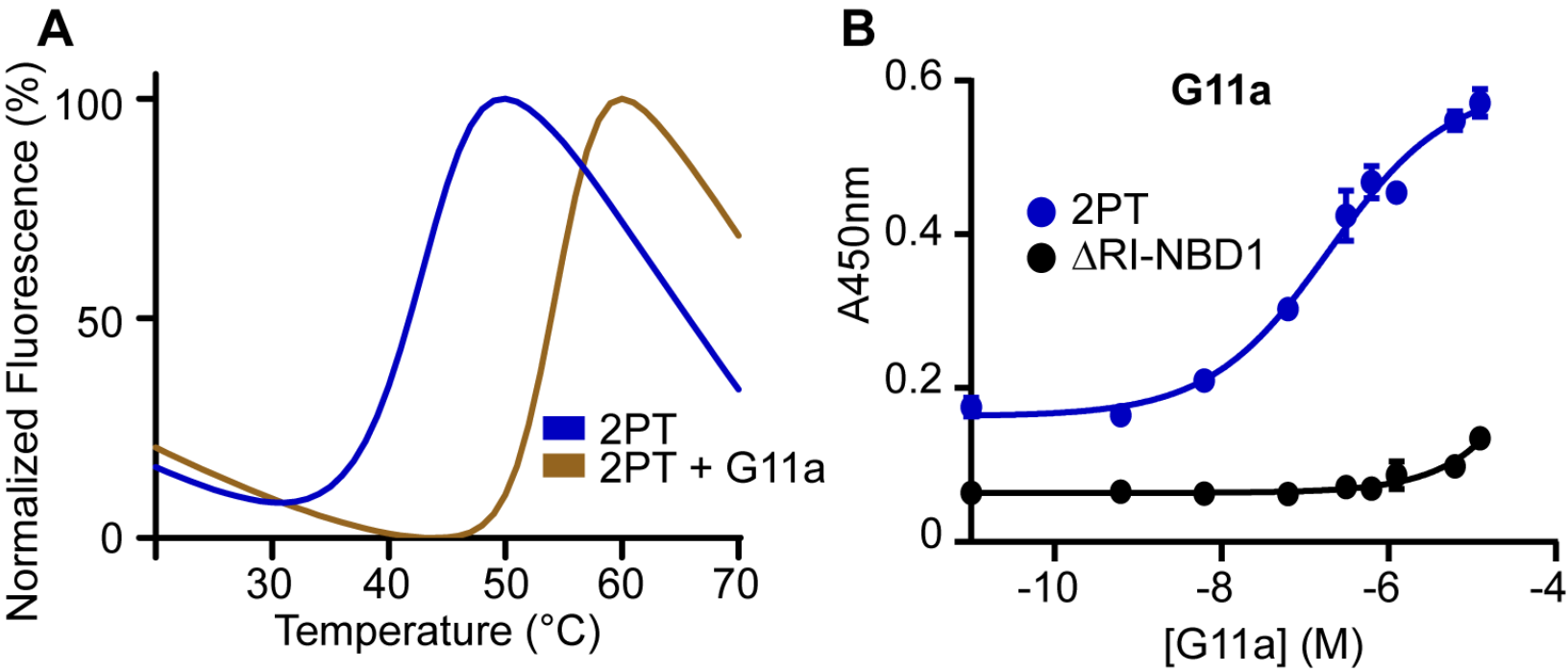
A
Normalized Fluorescence (%)
100
50
0
30
40
50
60
70
Temperature (°C)
2PT
2PT + G11a
B
G11a
A450nm
0.6
0.4
0.2
0
2PT
ΔRI-NBD1
-10
-8
-6
-4
[G11a] (M)

A ATTO488 and Alexa647 on 426-519 (β-SS conformation)

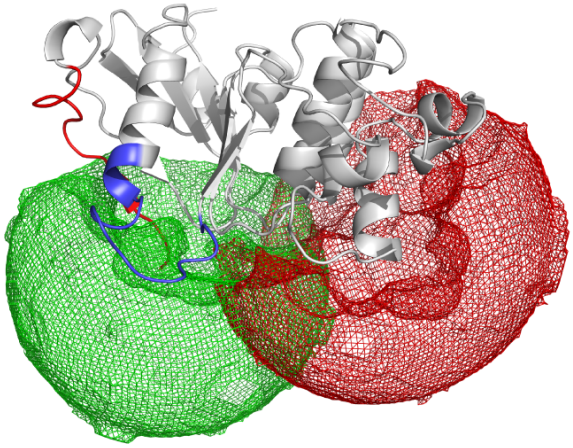

predicted $\langle R_{DA} \rangle$ = 35.0 ± 11Å
predicted E_{FRET} = 0.89

B ATTO488 and Alexa647 on 479-519 (2BBO)

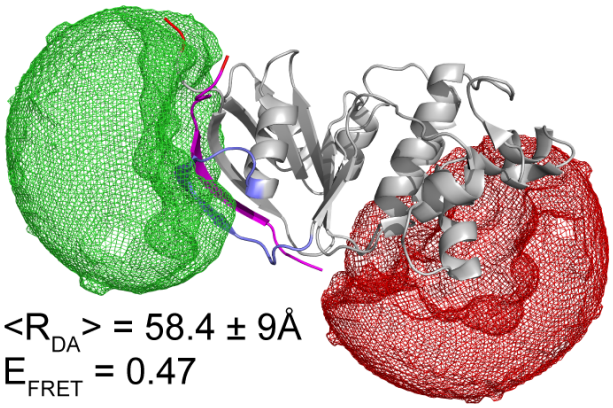

predicted $\langle R_{DA} \rangle$ = 58.4 ± 9Å
predicted E_{FRET} = 0.47

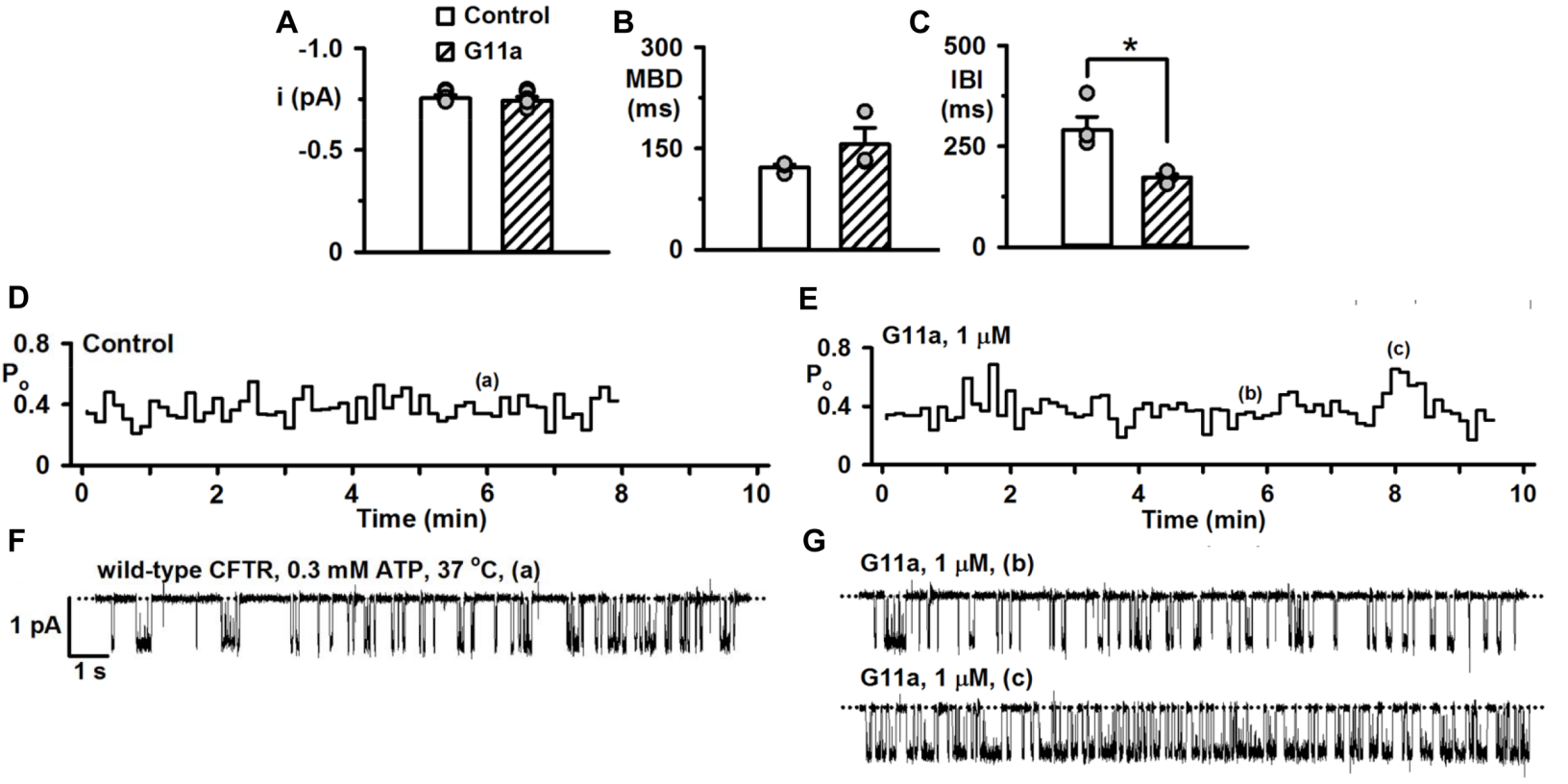
A
Control
G11a
-1.0
i (pA)
-0.5
0
B
300
MBD
(ms)
150
0
C
500
IBI
(ms)
250
0
*
D
0.8
Po
0.4
0
Control
(a)
0
2
4
6
8
10
Time (min)
E
0.8
Po
0.4
0
G11a, 1 μM
(b)
(c)
0
2
4
6
8
10
Time (min)
F
wild-type CFTR, 0.3 mM ATP, 37 °C, (a)
1 pA
1 s
G
G11a, 1 μM, (b)
G11a, 1 μM, (c)

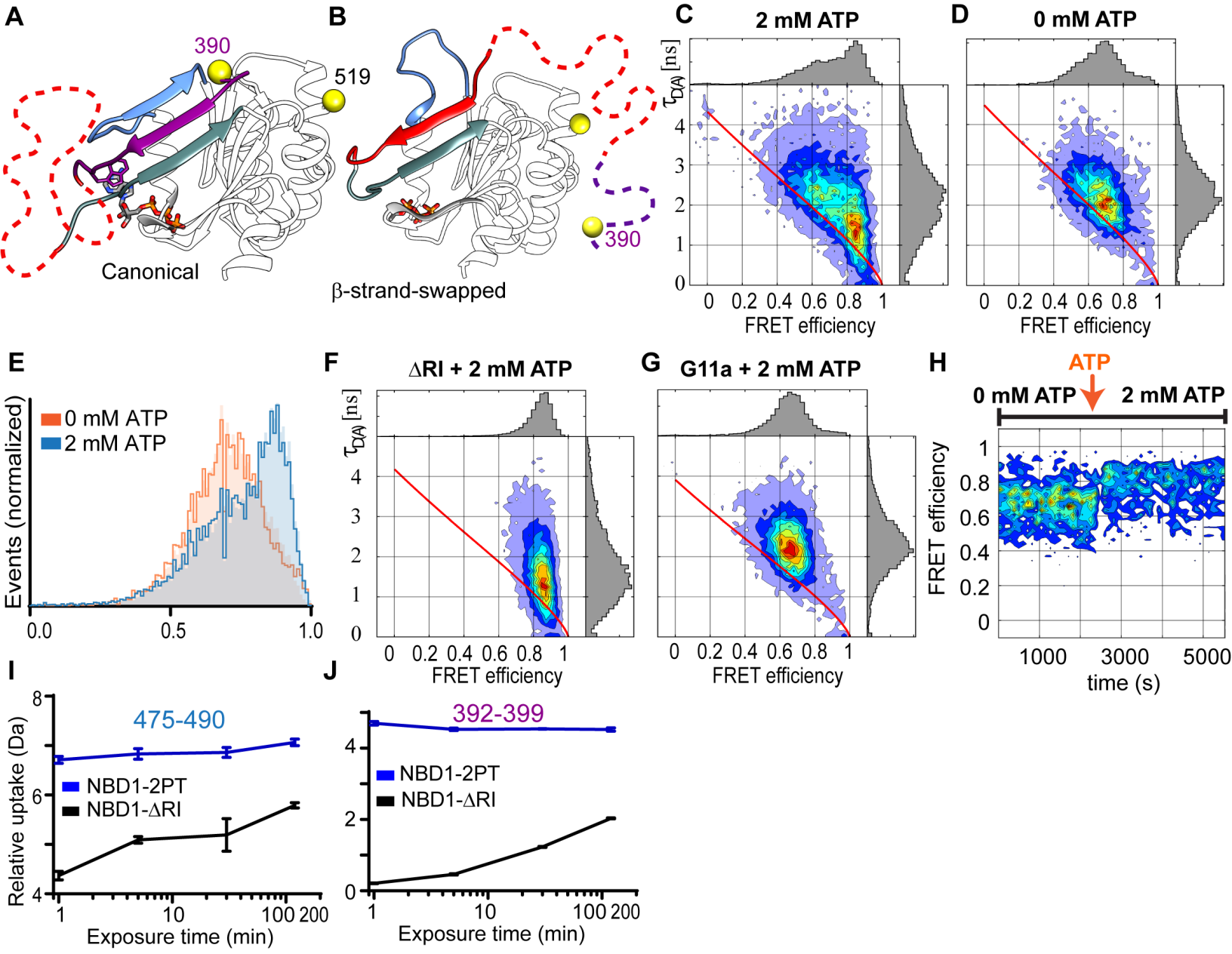
A
390
519
Canonical
B
390
β-strand-swapped
C
2 mM ATP
$\tau_{D(A)}$ [ns]
FRET efficiency
D
0 mM ATP
FRET efficiency
E
0 mM ATP
2 mM ATP
Events (normalized)
F
ΔRI + 2 mM ATP
FRET efficiency
G
G11a + 2 mM ATP
FRET efficiency
H
ATP
0 mM ATP
2 mM ATP
FRET efficiency
time (s)
I
475-490
NBD1-2PT
NBD1-ΔRI
Relative uptake (Da)
Exposure time (min)
J
392-399
NBD1-2PT
NBD1-ΔRI
Exposure time (min)

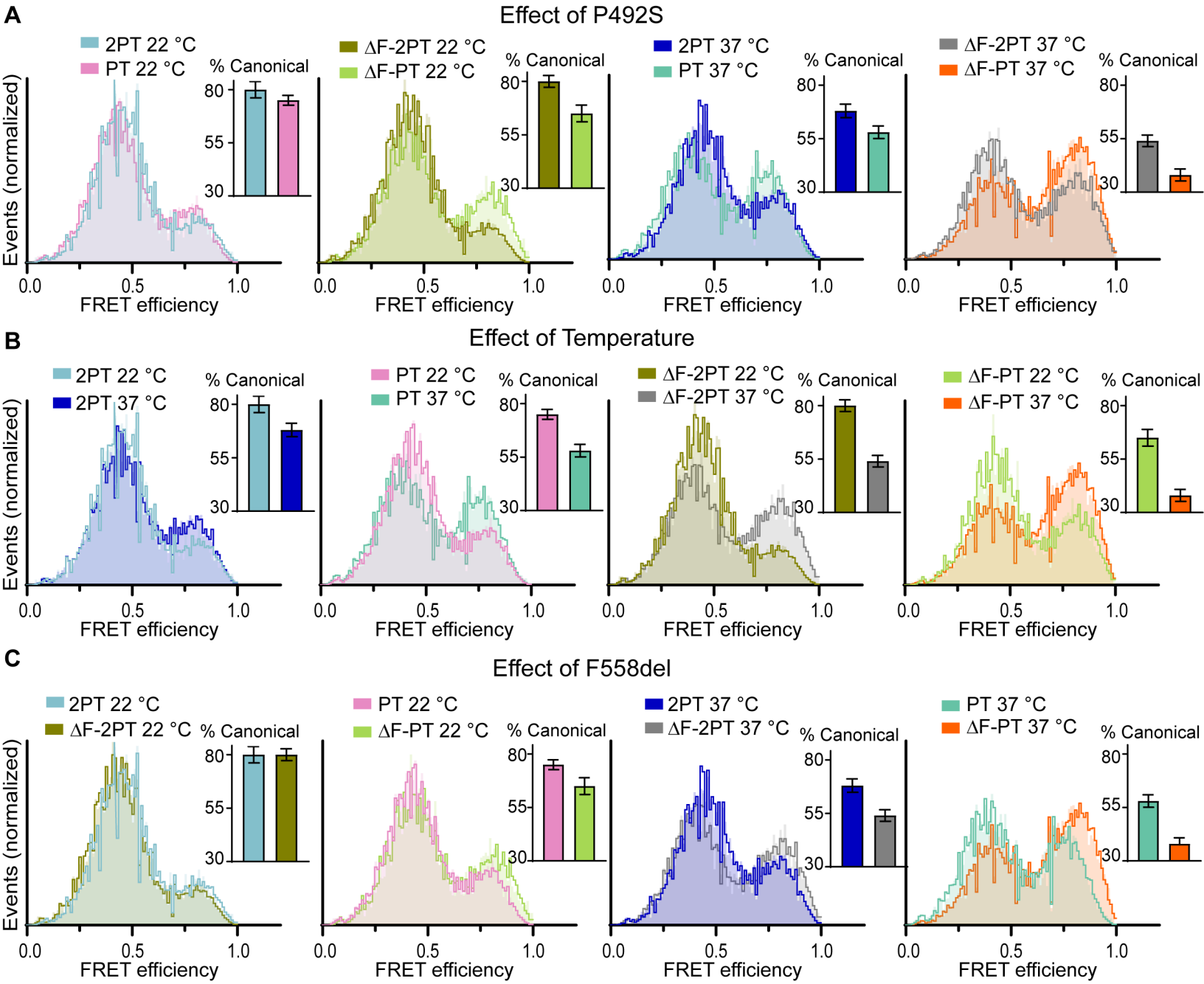
A
Effect of P492S
2PT 22 °C
PT 22 °C
% Canonical
ΔF-2PT 22 °C
ΔF-PT 22 °C
2PT 37 °C
PT 37 °C
ΔF-2PT 37 °C
ΔF-PT 37 °C
Events (normalized)
FRET efficiency
B
Effect of Temperature
C
Effect of F558del

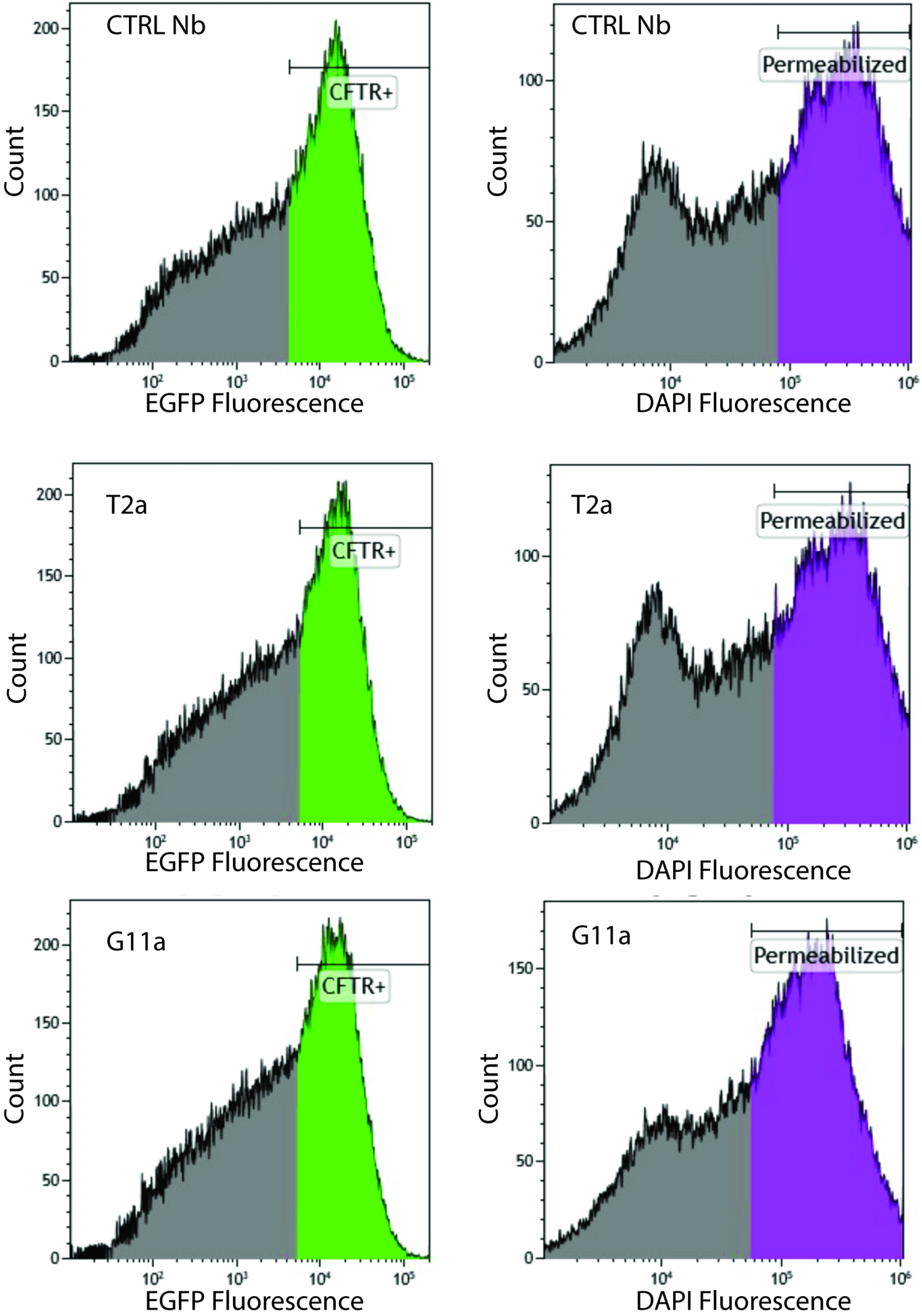
CTRL Nb
CFTR+
Count
EGFP Fluorescence
CTRL Nb
Permeabilized
Count
DAPI Fluorescence
T2a
CFTR+
Count
EGFP Fluorescence
T2a
Permeabilized
Count
DAPI Fluorescence
G11a
CFTR+
Count
EGFP Fluorescence
G11a
Permeabilized
Count
DAPI Fluorescence